

# Discovery of $\sim 9,000$ new RR Lyrae in the Southern Catalina Surveys

G. Torrealba<sup>1,2</sup>, M. Catelan<sup>1,3</sup>, A.J. Drake<sup>4</sup>, S.G. Djorgovski<sup>4</sup>, R.H. McNaught<sup>5</sup>,  
V. Belokurov<sup>2</sup>, S. Koposov<sup>2</sup>, M.J. Graham<sup>4</sup>, A. Mahabal<sup>4</sup>, S. Larson<sup>6</sup>,  
and E. Christensen<sup>5</sup>

<sup>1</sup>*Instituto de Astrofísica, Pontificia Universidad Católica de Chile, Av. Vicuña Mackena 4860, 782-0436 Macul, Santiago, Chile*

<sup>2</sup>*Institute of Astronomy, Madingley Rd, Cambridge, CB3 0HA*

<sup>3</sup>*Millennium Institute of Astrophysics, Santiago, Chile*

<sup>4</sup>*California Institute of Technology, 1200 E. California Blvd, CA 91225, USA*

<sup>5</sup>*The Australian National University, Siding Spring Observatory, Coonabarabran, NSW, Australia*

<sup>6</sup>*The University of Arizona, Department of Planetary Sciences, Lunar and Planetary Laboratory, 1629 E. Tucson AZ 85721, USA*

Accepted for publication in MNRAS 2014 October 28. Received 2014 October 8; in original form 2014 March 27

## ABSTRACT

We present the results of a deep, wide-area variability survey in the Southern hemisphere, the first of its kind. As part of the Catalina Sky Surveys, the Siding Spring Survey (SSS) has covered 14,800 square degrees in the declination range of  $-75^\circ \leq \delta \leq -15^\circ$ . To mine the enormous SSS dataset efficiently we have developed two algorithms: Automatic Period Selection (APS) and Automatic Fourier Decomposition (AFD), which aim to sharpen the period estimation and produce robust lightcurve models. Armed with the APS and AFD outputs we classify 10,540 ab-type RR Lyrae (RRab) stars ( $\sim 90\%$  of which are new) across the Southern sky. As well as the positional information we supply photometric metallicities, and unreddened distances.

For the RRab stars in the halo, a study of the photometric metallicity distribution reveals a nearly Gaussian shape with a mean metallicity of  $[\text{Fe}/\text{H}] = -1.4$  dex and a dispersion of 0.3 dex. A spatial study of the RRab metallicities shows no significant radial gradient in the first  $\sim 7$  kpc from the Galaxy center. However, further out, a small negative gradient is clearly present. This is complemented by a very obvious correlation of the mean RR Lyrae metallicity with distance above the Galactic plane,  $z$ . We have also carried out an initial substructure search using the discovered RRab, and present the properties of the candidates with significance greater than  $2\sigma$ . Most prominent among these is a southern extension of the Sagittarius dwarf galaxy’s stream system, reaching down to declinations  $\sim -40$  deg.

**Key words:** stars: variables: RR Lyrae – Galaxy: halo – Galaxy: structure – methods: statistical – methods: data analysis.

## 1 INTRODUCTION

The search is on to identify the fragments of those dwarf satellites that fell into the Milky Way many Gyrs ago. Even the most massive of these unfortunate galaxies must have had their star-formation throttled rather rapidly as the halo appears to be dominated by the old and metal-poor population (see e.g. Tolstoy et al. 2009). Scattered over hundreds of kiloparsecs, these low surface brightness tidal debris are outnumbered by the much closer disc and bulge stars with a ratio of at least 100:1. Luckily, the halo archetypical constituent, the RR Lyrae are easily recognized even at faint magnitudes provided that their lightcurves are mea-

sured with sufficient precision. Indeed, these old pulsating horizontal-branch stars have long been used as fundamental distance probes, shedding flickering light on the history of the Galaxy formation (e.g., Catelan 2009, and references therein).

Within the generally accepted  $\Lambda$ CDM paradigm, the formation of the stellar halo reflects the evolution of the shadowy one, made of dark matter. Both are assembled through the action of gravity mostly, but the links between the two are complex and their subtleties are only starting to be explored (e.g. Deason et al. 2013). Even if the “uniqueness” of the Milky Way is often viewed as both virtue and

vice, its place as a laboratory to study the structure formation in the low-mass regime is not contested. Only here, at home, the fine details of the hierarchical processes driven by the gravitational forces of the large-scale distribution of cold dark matter can be scrutinized with ample resolution and rigor (see e.g. Freeman & Bland-Hawthorn 2002). As shown by both data and simulations (e.g. Weisz et al. 2014; Brooks & Zolotov 2014), the lives of the accreted dwarfs are always severely affected. Even if some of them survive, their gas is stripped and as a result their star-formation hindered or altogether put out. Recently, such cinders of ancient star-formation have been uncovered within the Galactic halo in large numbers (Willman 2010; Belokurov 2013). While it is still not possible to compare directly the properties of the observed and the simulated dwarf satellites, it appears that the number of puzzling discrepancies is slowly growing (see e.g. Klypin et al. 1999; Bovill & Ricotti 2011; Boylan-Kolchin et al. 2011).

It is predicted that if the Galactic tides are strong enough, the infalling dwarf satellites are pulled apart leaving trails of stars that can be recognized as coherent overdensities in the halo (e.g., Johnston et al. 1996; Harding et al. 2001). With the advent of deep all-sky surveys, the examples of prehistoric and ongoing disruption events have been seen all around the Galaxy (e.g., Vivas et al. 2001; Newberg et al. 2002; Majewski et al. 2003; Belokurov et al. 2006; Grillmair 2006; Belokurov et al. 2007a,b; Drake et al. 2013a). Despite the abundance of the Galactic tidal debris detections, a detailed quantitative comparison with state-of-the-art numerical simulations has not yet been carried out. Curiously, the few studies that do attempt to gauge the lumpiness of the Milky Way stellar halo in both real and mock datasets, tend to conclude that the Galaxy is somewhat smoother than predicted (see e.g. Helmi et al. 2011; Deason et al. 2011). This might simply be because the total stellar mass in the myriad of the recently discovered sub-structures is relatively small. Such estimates of the halo lumpiness rely of course on the knowledge of the global properties of the stellar halo, including its integrated luminosity and overall extent. These, however, are poorly determined, as large portions of the Galaxy remain unexplored: the most obvious lacunae being the low-latitude inner portions of the halo as well as large swathes of the Southern sky.

The Catalina Sky Survey has collected multi-epoch imaging data from three different observing sites, covering most of the accessible sky, namely the area from  $\delta = -75^\circ$  to  $\delta = +65^\circ$ . The Survey’s results in the Northern hemisphere have been presented recently Drake et al. (2013a,b). Here, we analyse data from the Southern hemisphere segment of Catalina, the Siding Spring Survey (SSS). The aim of our analysis is to fill in the obvious gap in the South, and discover and characterize ab-type RR Lyrae stars with  $-75^\circ < \delta < -15^\circ$ . RR Lyrae stars, and in particular those of the ab-type (RRab), have long been known as a trusted tracer of the Galactic halo. The RRab’s are relatively easy to differentiate from other types of variable stars due to the characteristic asymmetric shape of the lightcurve. We, therefore, concentrate solely on RRab’s which allows us to assemble a comparatively clean sample of stars over  $\sim 14,800$  square degrees. As a result, when combined with the previously published Catalina Sky Survey catalogues, our total

RR Lyrae sample covers more than 33,000 square degrees and reaches distances in excess of 50 kpc.

Thanks to the immense, un-interrupted spatial extent of our survey, we can, for the first time, build a global inventory of the halo sub-structures. Most importantly, it is now possible to quantify large-scale asymmetries (e.g. Pawlowski et al. 2012) if any are indeed present. Recently, several bloated halo structures covering hundreds of square degrees have been identified in the Northern sky, including the Hercules-Aquila Cloud (HAC; Belokurov et al. 2007a) and Virgo Overdensity (VOD; Vivas et al. 2008; Jurić et al. 2008). In their morphology, these stellar “clouds” are distinct from narrow tidal tails or “streams”, and were likely produced as a result of nearly radial in-fall of relatively massive galaxies, but their exact origin is still unknown. With the data from one half of the sky missing, it has been impossible so far to establish whether several large inner halo structures are connected in any way. Given that both Virgo (see e.g. Duffau et al. 2014) and HAC (Simion et al. 2014) contain copious amounts of RR Lyrae, we hope that our new sample will help to complete the puzzle.

Finally, we also hope to leverage thousands of precise distances across the Southern sky to understand better the most prominent un-relaxed structure in the outer Galaxy, the Sagittarius stream. The Sagittarius dwarf spheroidal galaxy (Ibata et al. 1994) and its associated tidal tails (see e.g. Majewski et al. 2003) are probably the best-studied example of the Galactic halo sub-structure. However, after two decades and dozens of published papers (see e.g. Jiang & Binney 2000; Fellhauer et al. 2006; Law & Majewski 2010; Yanny et al. 2009; Koposov et al. 2012; Belokurov et al. 2014b) there remain many unanswered questions about the Sgr accretion event. The Sgr stream is so long that its wraps overlap in many locations on the sky thus confusing the interpretation. Our data possesses the necessary accuracy to resolve the sub-structure along the line of sight, therefore helping to untangle Sgr’s intertwined tidal tails.

The main objective of this paper is to automate the RR Lyrae catalog production. Therefore, we start by introducing the survey data in Section 2 and then go on to describe the algorithms designed to find and classify the RRab in Section 3. In Section 4 we give the details of the calculation of the RRab fundamental parameters. Finally, the properties of the discovered RRab stars are presented in Section 5.

## 2 DATA AND CALIBRATION

In this paper we analyze 18,288 periodic variable candidates found in the SSS, the Southern part of the Catalina Sky Survey. The Catalina Sky Survey began in 2004 and utilized three telescopes at three different observing sites to cover the sky between declination  $-75^\circ < \delta < +65^\circ$ . Acquiring images of the sky across more than 33,000 square degrees, the principal aim of the Catalina Sky Survey was to discover Near-Earth Objects (NEOs) and Potential Hazardous Asteroids (PHAs; Larson et al. 2003). Its counterpart, the Catalina Real-time Transient Survey (CRTS), involves the analysis of the same data in order to detect and classify stationary optical transients (Drake et al. 2009). Both surveys work collaboratively to extract the maximum scien-

tific return from the data of the three telescopes operated by the Catalina Sky Surveys. These consist of the Catalina Schmidt Survey (CSS) telescope, the Mount Lemmon Survey (MLS) telescope, and the SSS telescope in Siding Spring, Australia. Each telescope is equipped with a  $4k \times 4k$  CCD camera, with the field of view of 8.2, 1.1 and 4 square degrees for the CSS, MLS and SSS, respectively. The focus of this work, the SSS uses the Uppsala 0.5-m Schmidt telescope equipped with a CCD camera nearly identical to the one used by its northern counterpart, the CSS, which is an obvious advantage in terms of homogeneity of the resulting photometry. The pixel size is 2 arc minutes giving a field of view of 4 square degrees. In the SSS observations, the Galactic plane region ( $|b| < 15^\circ$ ) is avoided due to crowding. Images are unfiltered to maximize throughput, and taken in sequences of four observations separated by ten minutes with exposures that last approximately 30 seconds. SExtractor (Bertin & Arnouts 1996) is employed to obtain photometry of individual objects in an automated fashion.

The initial selection of variable objects and the subsequent photometric transformations are all part of the general Catalina pipeline and are identical to those described in Drake et al. (2013a), and therefore are only briefly summarized here. First, variable source candidates were identified from the SSS data using the Welch-Stetson variability index  $I_{ws} > 0.6$  (Welch & Stetson 1993). Then, for all objects in the list of potential variables, the Lomb-Scargle period finding method (Lomb 1976; Scargle 1982) was applied and periodic variable candidates with periods between 0.1 and 4 days were selected. These boundaries are chosen to be broader than the expected range of periods for RRAb stars ( $\sim 0.4 - 1$  days) to make sure that we also recover RRAb stars affected by aliasing in the Lomb-Scargle analysis. The sample of periodic variables consists of  $\sim 20,000$  objects with unfiltered magnitudes between 10.5 and 19.2 and  $\sim 100$  epochs each. Figure 1 shows locations of all candidate periodic objects in equatorial coordinates, to give an idea of the spatial extent of the sample.

Since the CCD used by the SSS matches closely the one used by the CSS (implying, of course, that the responses are nearly identical), we can apply the calibration equations implemented by the CSS to transform between the unfiltered Catalina SSS data and the standard Johnson  $V$  filter. This is given in equation 1 of Drake et al. (2013a):

$$V = V_{SSS} + 0.31(B - V)^2 + 0.04. \quad (1)$$

This relation has a dispersion of  $\sigma = 0.059$  mag. Since in this work we focus on RRAb stars, we investigate the impact of color variations on the recovered properties of these variables. If we consider an average color for RRAb stars of  $(B - V) \sim 0.3$  mag and the possible color range of  $0.1 \text{ mag} \lesssim (B - V) \lesssim 0.5 \text{ mag}$  (Guldenschuh et al. 2005), the maximum difference in color is  $\sim 0.2$  mag in  $(B - V)$ . This adds an extra uncertainty of  $\sim 0.05$  mag to eq. 1, which combined in quadrature with the dispersion of the relation gives a total dispersion of 0.077 mag in the  $V$  magnitude. However, because RRAb's change color during their pulsation cycle, taking the average color might cause measurable effects to the lightcurve shape, which in turn could lead to a bias in the estimation of the metallicity and the average magnitude of the star. We tested these effects by making

a simple model of the RRAb color change as a function of the lightcurve phase, following the typical color variations of the RRAb during their pulsation cycles as seen in Figure 2 of Guldenschuh et al. (2005). We used this model to transform the  $V_{SSS}$  mag to  $V$  mag as a function of phase and estimate the metallicity and the average magnitude. We then compared these quantities with the one obtained by taking a constant value of  $(B - V) = 0.3$  mag, and found that the differences have a dispersion of 0.05 dex for the metallicity and 0.004 mag for the average magnitude. These values are an order of magnitude smaller than the typical uncertainty induced by photometric error. Since we lack the color information in the SSS data, and given that the effects of the color variation over the pulsation cycle are small, we believe that we are justified in using an average color of  $(B - V) = 0.3$  mag to transform between  $V_{SSS}$  and Johnson  $V$ .

### 3 PERIOD DETERMINATION

Efficient detection of RRAb in a dataset like SSS is possible solely thanks to their characteristic lightcurve shapes. However, the asymmetry in the RRAb pulses only reveals itself if the lightcurve is phased (folded) with the correct period. Moreover, the metallicity and the intrinsic luminosity of such a variable star both require accurate lightcurve morphology measurements. Getting the period right is therefore absolutely crucial for both the identification of RR Lyrae as well as the subsequent inference of their properties. We tackle the problem of automating the RR Lyrae discovery and characterization by developing two routines, the Automatic Fourier Decomposition (AFD), which builds robust lightcurve models, and the Automatic Period Selection (APS), which makes use of different periodograms to home in on the correct period. With these tools in hand, the process of the classifying variables based on the shapes of their lightcurves is fast, robust and reproducible. In sections 3.1 and 3.2 the two routines are introduced and discussed in detail.

#### 3.1 Automatic Fourier Decomposition

The essence of the AFD method is that the complexity of the lightcurve model is dictated by the data's signal-to-noise ratio as well as the details of the lightcurve morphology. In other words, the number of harmonics in the Fourier decomposition of a phased lightcurve is increased as long as the fit continues to be statistically significant. To find the parameters of the harmonics in the Fourier decomposition we carry out a weighted least-squares fitting procedure where the model lightcurve is described by:

$$f(x) = A_0 + \sum_{n=1}^{n_{max}} A_n \sin\left(\frac{2n\pi t}{P} + \phi_n\right), \quad (2)$$

where  $A_n$  are the amplitudes,  $\phi_n$  the phases,  $P$  the period and  $n_{max}$  the number of harmonics in the decomposition. To determine the value of  $n_{max}$ , we perform several fits with increasing number of harmonics until it is not statistically significant to add an extra harmonic. The process starts with just one harmonic:

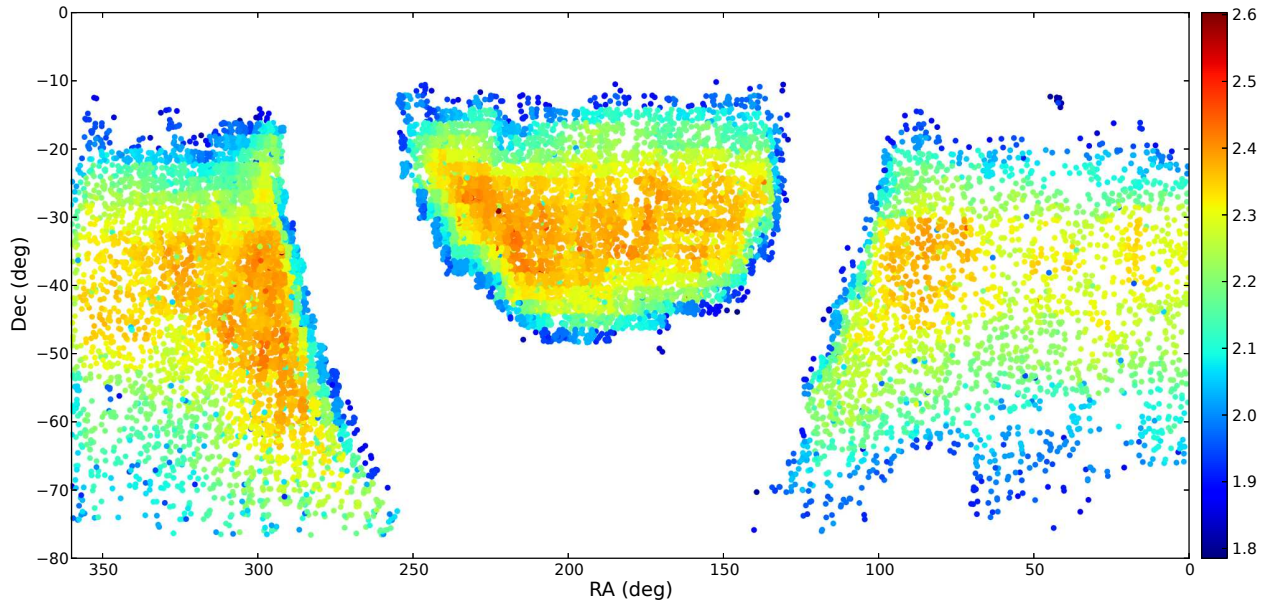


**Figure 1.** Spatial extent of the SSS sample in equatorial coordinates. Each filled circle is a candidate periodic variable as selected by the Catalina pipeline. The color represents the logarithm of the number of observations, as indicated by the scale on the right. Note the drop in frequency of visits close to the edges of the survey.

$$f(x) = A_0 + A_1 \sin\left(\frac{2\pi t}{P} + \phi_1\right). \quad (3)$$

We perform a least-squares fit to determine  $A_0$ ,  $A_1$ , and  $\phi_1$ , and quantify the goodness of the fit through the reduced  $\chi^2$  statistic, calculated as follows:

$$\chi^2 = \frac{1}{N - n - 1} \sum_{k=1}^N \left( \frac{O_k - E_k}{\sigma_k} \right)^2, \quad (4)$$

where  $N$  is the number of observations,  $n$  the number of parameters of the Fourier decomposition,  $\sigma$  the error of the observation,  $O$  the observed value, and  $E$  the expected value as given by the Fourier series. We then compare the quality of this fit to a Fourier decomposition with one extra harmonic and with two extra harmonics. To determine if the series with extra harmonics gives us a significant improvement on the quality of the fit, we perform a statistical F-test to check if the null hypothesis (i.e., the two fits are statistically equal in terms of their performance) can be discarded. The  $F$  statistic is calculated as follows:

$$F = \left( \frac{\chi_1^2}{\chi_2^2} - 1 \right) \frac{b}{a}, \quad (5)$$

where  $b = N - p_2$  is the number of degrees of freedom of the second fit, and  $a = p_2 - p_1$  is the difference in the number of parameters  $p$  between the second and the first fit (note that  $p_2 > p_1$  always). The test statistic is then compared to a critical value,  $\alpha$ ; if  $F$  is less than the critical value, the null hypothesis cannot be discarded and the two models are statistically equal in their ability to describe the observed data. To determine  $\alpha$ , we require that the rejection probability is

0.99, that is, the null hypothesis is discarded when we are 99% sure that adding a new order to the series is statistically significant. In addition to this, we set the maximum number of harmonics to 6, to avoid over-fitting. In Figure 2 we show three lightcurves that were fit by the AFD with different number of harmonics. It is reassuring to see that in each case, the algorithm appears to have set the series truncation according to the complexity of the lightcurve.

### 3.2 Automatic Period Selection

APS makes period estimation given the available multi-epoch data more robust. Our approach is to compare periods singled out by different period finding algorithms and quantify the goodness of fit by applying the AFD lightcurve model (see Section 3.1). In particular, we compare the periods proposed by two algorithms, namely Analysis Of Variance (AOV; Schwarzenberg-Czerny 1989, 1996; Schwarzenberg-Czerny & Beaulieu 2006) and Lomb-Scargle Periodogram (LS; Lomb 1976; Scargle 1982). The comparison is done by phasing the lightcurve with the five best periods proposed by each routine and calculating the goodness-of-fit parameter to discriminate between the periods and converge on the best one. Since the SSS photometry occasionally has some spurious measurements, we apply a simple cleaning routine by removing the most obvious outliers. In order to do this, we find the mean magnitude and the overall amplitude of the lightcurve from an initial AFD and remove all datapoints that lie more than  $3\sigma$  from the mean, where  $\sigma$  is the standard deviation of the mean lightcurve magnitude. With the outliers removed we then perform a second AFD run. Figure 3 displays both the first AFD model as well as the result of the second AFD run after the outliers

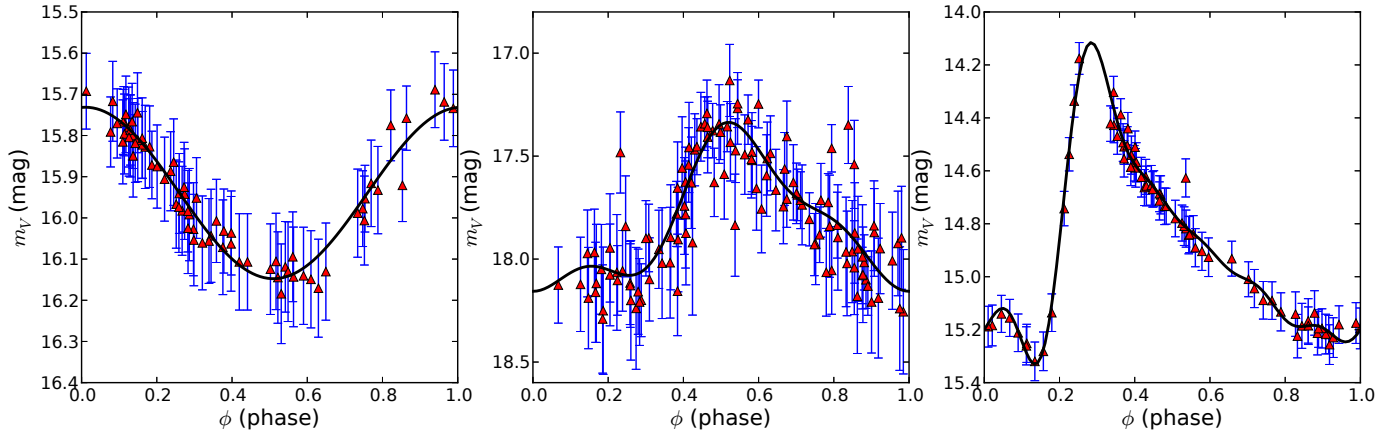


**Figure 2.** Illustration of the AFD lightcurve fitting (see text for more detail). This shows three examples of phased lightcurves (red triangles show the SSS photometric data, while the associated error-bars are shown in blue) of three different periodic variables as well as their AFD models (black curves). From Left to Right: examples of lightcurves that are well fit with two (left), four (middle), and six (right) Fourier harmonics, respectively.

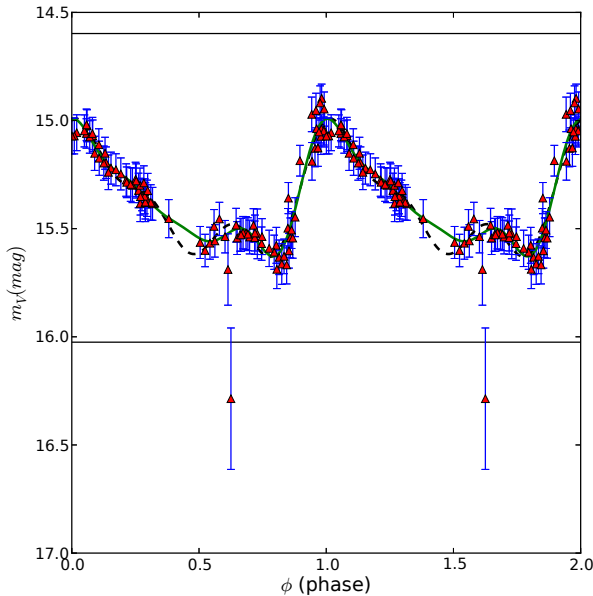


**Figure 3.** Impact of the first sigma clipping on model selection. The dashed black line represents the AFD model without sigma clipping, while the green line shows the AFD fit after sigma clipping. Horizontal black lines give the threshold,  $3\sigma$  away from the mean, outside which the data is clipped. The impact of the outlier present at  $\phi \sim 0.1$  is clearly visible as the model shown by black dashed line is “pulled” towards the discrepant datapoint.

(i.e. datapoints above the sigma-clipping limits shown) have been removed.

Additionally, there are two extra processes to further clean the lightcurve if need be: the conventional outlier clipping and the so-called gap-filling. Note, however, that the clipping algorithm does not work well on lightcurves of deep eclipsing binaries, but can, in principle, be applied to RR Lyrae variables. The process consists of clipping all datapoints of the lightcurve that lie more than  $3\sigma$  from the re-

cently computed AFD model at a given phase, rather than from the overall mean of the lightcurve. In this case,  $\sigma$  is the mean error of the observations. Figure 4 shows the lightcurve clipping boundaries and how these can be used to excise some of the outliers that have survived the first cut. The gap-filling process is triggered when there is a gap of more than 0.1 in the lightcurve phase. When this condition is satisfied, a “data” point is included in the lightcurve based on the previously calculated AFD. The synthetic observation is positioned according to a simple linear interpolation between the phase values at the edges of the gap. The interpolation points are chosen as the mean of the three points closest to the edges on each side of the gap (in phase space). This process relies on the previous AFD run to assign the appropriate magnitudes around the edge. As seen in Figure 5, this helps to remove extreme wriggles from the model lightcurve. The post-processing techniques described above are used to improve the lightcurve shape estimation when applying the AFD. Subsequently, we utilize the AFD goodness-of-fit to discriminate between possible test periods.

To select the best period the following rules are applied. First, if two period candidates have a difference of more than 10% in reduced  $\chi^2$ , the best period is selected. If this condition is not met, but the two first candidates of AOV and LS are similar (i.e. their difference is lower than  $10^{-3}$  days), and match one of the two best periods ranked by the reduced  $\chi^2$  test, that period is selected. If neither of the two criteria is met, but the first two periods are aliases (either double or half the period), then, since the AOV periodogram is able to damp the detection sensitivity for aliased periods (Schwarzenberg-Czerny 1996), the one ranked higher by AOV is chosen. Finally, if neither of these conditions is met, the star is flagged as having a problematic period. We also flag stars with reduced  $\chi^2 > 3$  and those with periods greater than 4 days, since given the pre-selection condition mentioned in §2, we do not expect to find stars with periods that long, and they are usually associated with spurious period candidates. The  $\chi^2$  distribution of the accepted lightcurves peaks at  $\sim 0.3$  rather than 1. There are several possibilities to explain the location of the peak. First, the

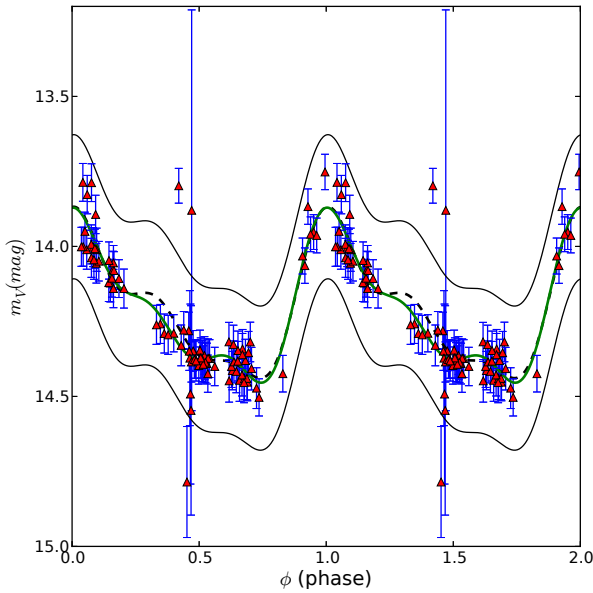


**Figure 4.** Same as Figure 3, but for a different method of clipping. Here, instead of discarding all datapoints that are outside a fixed range given by the mean and the standard deviation of the lightcurve measurements, a sliding threshold is used. At each phase, the clipping threshold is calculated with respect to the value of the previous AFD model fit. The effect of the datapoints outside the accepted region is less important than in the aforementioned plain sigma-clipping process, but these can add noticeable wriggles to the AFD fit as illustrated by the differences between the black dashed line (before clipping) and the green solid line (after clipping).

error of the SSS observations might be overestimated. Second, we might be over-fitting the lightcurves, and finally, of course, there could be a combination of the first two. While overfitting is difficult to avoid in some cases, we point out that the main point of the AFD is to avoid this and provide better lightcurve characterizations at the same time. Therefore, we believe that the peak value of the  $\chi^2$  distribution might be due to a combination of an overestimation of the errors of the observations, and somewhat over-zealous removal of the outliers which are, of course, the main causes of high  $\chi^2$ .

Finally, we test the performance of the APS algorithm on  $\sim 1000$  randomly chosen phased lightcurves. Visual inspection of this sub-set confirms that the method can correctly select the periods when both AOV and LS agree, when they do not agree, and even when they both fail with their most significant period candidate. Note that, in order to avoid contamination, we have made this method very restrictive. In other words, if the  $\chi^2$  test cannot tell the difference between the two best period candidates, we leave the star out of the sample. This culls only of order of 6% of the sample. Combined with the stars that could not be modeled with the AFD (i.e., reduced  $\chi^2 > 3$ ), and the stars with periods in excess of 4 days, the total number of rejected lightcurves is of order of 10%. This is a reasonably small price to pay, provided we achieve reliable period estimation for the remaining  $\sim 90\%$  of the stars. We believe, based on

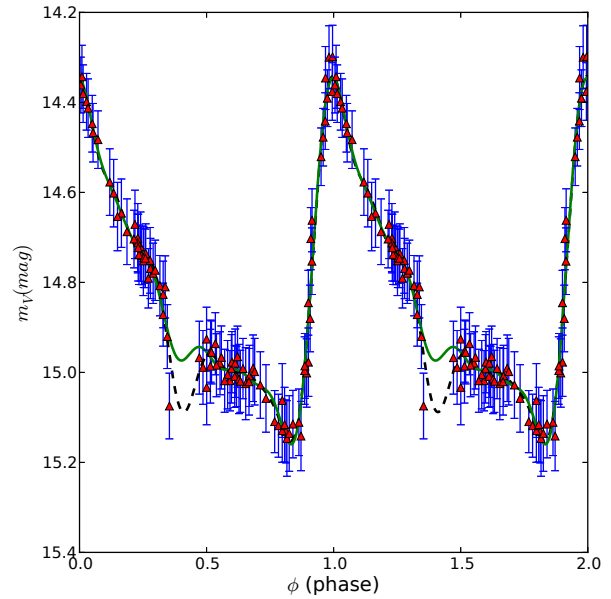


**Figure 5.** Illustration of the gap filling procedure. Red triangles show the SSS photometry at each phase for a chosen period, and the associated errors are in blue. Black dashed (green solid) line displays the AFD model before (after) the gap filling. As with lightcurve clipping, the effect of this procedure is secondary in comparison to the raw sigma clipping process, but removes considerable wriggles from the AFD.

the test described above, that out of these only  $\sim 1\%$  have wrong periods.

## 4 SELECTION OF RRAB. DISTANCE AND METALLICITY INFERENCE

### 4.1 The M Test

Armed with the period and the lightcurve shape information, we proceed to select the most likely RRab stars from the sample of variable objects. Note that all objects flagged to have unreliable periods (as described in the previous sections) are removed, which leaves a total number of 16,500 candidates. Within the period range occupied by RRab's, the other common periodic variables are eclipsing binaries. To differentiate between pulsating and eclipsing stars, we introduce the M-test, a simple lightcurve shape statistic motivated by Kinemuchi et al. (2006), and already utilized in Drake et al. (2013a,b). This is defined as follows:

$$T_m = \frac{M_{max} - M_{mean}}{M_{max} - M_{min}}, \quad (6)$$

where M denotes magnitude. In essence, the M-statistic  $T_m$  measures the amount of time the star spends above ( $T_m > 0.5$ ) or below ( $T_m < 0.5$ ) a baseline defined by the mean magnitude. To mitigate the destructive action of outliers, all parameters used to calculate  $T_m$  are extracted from the AFD model. This is the principal difference with the original method as proposed by Kinemuchi et al. (2006), where the actual lightcurve data is used to calculate the M-



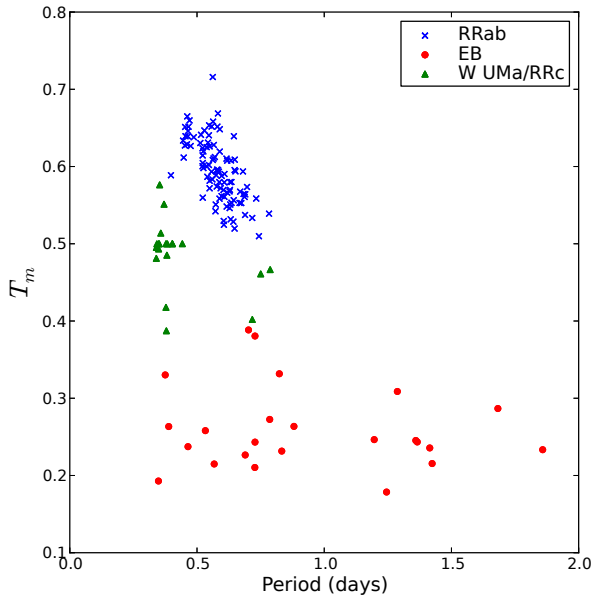


**Figure 6.** M-statistic as a function of the variable star period for a small sub-sample of objects inspected visually. Blue crosses are confirmed RRab stars, green triangles are possible RRc and/or W UMa variables, while red filled circles are eclipsing binaries (excluding W UMa systems). This figure clearly demonstrates how this simple lightcurve symmetry statistic helps to discriminate between the RRab stars and the rest of the variables.

statistic. Different types of variables occupy different positions, in a period vs.  $T_m$  diagram. To determine the exact boundaries of the different classes in this plane,  $\sim 150$  randomly selected variables were classified by eye into three groups: RRab's, detached eclipsing binaries and RRc/W UMa- type eclipsing binaries. Figure 6 shows the locations of these groups in period- $T_m$  space. As is obvious from this figure, RRab's form a tight and fairly isolated group with high values of the M-statistic. To further clean our sample, we removed all lightcurves that have more than one peak in phase space. This is achieved by tagging all the stars whose amplitude in the higher harmonics of the AFD model is larger than the amplitude of the first harmonic. With regards to the RR Lyrae of c type, there possibly exists a region in Figure 6, i.e. at low periods and intermediate  $T_m$ , which is predominantly populated by these pulsators. However, the levels of contamination with W UMa stars are still high. Accordingly, in order to have the simplest and the cleanest selection possible, we do not attempt to disentangle RRc's and W UMa's, and focus on RRab stars only. Table 1 gives a summary of all selection cuts imposed to identify RRab stars.

#### 4.2 Photometric Metallicities and Absolute Magnitudes

Photometric metallicities for the stars in our sample are based on the relation established in Jurcsik & Kovács (1996):

$$[\text{Fe}/\text{H}]_j = -5.038 - 5.394 P + 1.345 \phi_{31}, \quad (7)$$

**Table 1.** Discrimination criteria used to select RRab type stars.

Criteria	Limits
Period	0.4 – 1.0 days
$n_{max}$	$\geq 3$
Amplitude	$\leq 2$ mag
$T_m$	$\geq 0.5$

Notes:  $n_{max}$  is the number of Harmonics used by the AFD, and  $T_m$  is the value of the M-statistic as given by equation 6.

where  $P$  is the period in days,  $\phi_{31} = \phi_3 - 3\phi_1$ , and the metallicity is given on the scale of Jurcsik (1995). It is important to note that, when computing the Fourier decomposition coefficients (eq. 2), we require that all amplitudes are positive and the phases are restricted to the range between 0 and  $2\pi$ . We transform the metallicity in equation 7 to the standard Zinn & West (1984) scale using equation 4 of Jurcsik (1995):

$$[\text{Fe}/\text{H}]_{ZW} = \frac{1}{1.431} \left( [\text{Fe}/\text{H}]_j - 0.88 \right), \quad (8)$$

which in turn can be transformed to the UVES high resolution spectroscopic scale of Carretta et al. (2009) using:

$$[\text{Fe}/\text{H}]_{UVES} = 1.105 [\text{Fe}/\text{H}]_{ZW} + 0.16. \quad (9)$$

To check the reliability of these metallicity estimates, we calculate the  $D_m$  factor (see Jurcsik & Kovács 1996, eq 6). Note that at least 6 orders in Fourier decomposition of the lightcurve are required to calculate this parameter. Many RRab stars in our sample have 3 or more orders in their AFD model. Therefore, we produce two  $D_m$  estimates, one using the available orders only (that we called  $D_{mp}$ ), and second forcing the AFD to have all 6 orders, as in the calculations originally made by Jurcsik & Kovács. Note that there are known issues with this metallicity estimate, as the relation tends to overestimate  $[\text{Fe}/\text{H}]$  at the metal poor end by  $\sim 0.3$  dex (see e.g. Nemec 2004; Smolec 2005).

Given the possibility that values based on the Jurcsik & Kovács (1996) expression can overestimate the RR Lyrae metallicity at the low end, it is worth considering possible alternatives to test the robustness of our results. Recently, a new period- $\phi_{31}$ -metallicity relation has been published by Nemec et al. (2013). The authors use the RR Lyrae in the *Kepler* satellite's field of view to establish the following transformation:

$$[\text{Fe}/\text{H}] = -8.65 - 40.12 P + 5.96 \phi_{31} + 6.27 P \phi_{31} - 0.72 \phi_{31}^2, \quad (10)$$

where  $P$  is the period of the star in days. Note that this relation uses the *Kepler*  $K_p$  system; therefore, it is necessary to transform it to the standard Johnson  $V$  by applying equation 2 of Nemec et al. (2011), i.e.  $\phi_{31}(V) = \phi_{31}(K_p) - 0.151(\pm 0.026)$ . Nemec et al. (2013) suggest that  $[\text{Fe}/\text{H}]$  values obtained in this way are in the UVES scale, but we have checked that, at intermediate metallicities (as applicable to most of the stars in our sample), they are also in good agreement with the  $[\text{Fe}/\text{H}]$  values provided by Jurcsik & Kovács (1996), accordingly, we compare them di-

rectly, which is the same approach that Nemec et al. (2013) uses to compare their results with Jurcsik & Kovács (1996)<sup>1</sup>. The relation has an intrinsic scatter of only 0.084 dex; however, we cannot carry out the conventional error propagation as no details of the covariance matrix are provided by the authors. This makes it impossible to gauge realistic errors for stars with poorly determined  $\phi_{31}$ . To this end, even when we use both scales to study the metallicity distribution in the halo, we must retain the Jurcsik & Kovács (1996) metallicity measures for the estimation of the RRab distances.

Given the metallicity, the absolute magnitude of a RRab star is calculated according to the following expression, from Catelan & Cortés (2008):

$$M_V = (0.23 \pm 0.04)[\text{Fe}/\text{H}]_{ZW} + (0.95 \pm 0.13), \quad (11)$$

which can be converted to obtain absolute magnitudes from the Carretta et al. (2009) scale using equation 9 to obtain:

$$M_V = (0.21 \pm 0.04)[\text{Fe}/\text{H}]_{UVES} + (0.92 \pm 0.13). \quad (12)$$

Finally, the unreddened magnitudes are obtained by applying the dust extinction corrections from the Schlegel et al. (1998) reddening maps. Note that the color excess,  $E(B - V)$ , might be overestimated for values greater than 0.15 mag (Arce & Goodman 1999). These values might be corrected by using the relation given in equation 1 of Bonifacio et al. (2000). Note, however, that these corrections are small ( $\sim 10\%$ ) for  $E(B - V) < 0.3$ . Since our stars are typically located in zones of high Galactic latitude, where the extinction is low, we do not take into account this effect. Nevertheless, we include the values of  $E(B - V)$  with the detected RRab's. lower than 0.3

### 4.3 Completeness and Reliability

To check the reliability of our algorithms, we generate synthetic lightcurves based on Layden (1998) RRab templates. To make the lightcurves as similar as possible to the ones observed by SSS, we studied how the error of the observations change with magnitude. Figure 7 shows the behaviour of the error with increasing apparent magnitude. To model the error evolution as a function of magnitude, an exponential model is used:

$$\sigma_M(M) = 0.04 + 1.84 \times 10^{-3} \exp(0.55[M - M_{min}]), \quad (13)$$

where  $M_{min} = 9.51$  corresponds to the brightest star in our sample. To generate the synthetic RRab, pulse amplitudes as well as phases of random stars in the sample are used; the errors are obtained from equation 13, and the noise is drawn from a normal distribution with sigma as given by equation 13. For each magnitude bin, 100 synthetic RRab are generated, in the range  $12 < V < 18$ . We then run the APS algorithm and count the number of mock RRab we can recover as a function of apparent magnitude. Figure 8 illustrates that at least 60% of the RRab with  $V = 18$  are recovered. The same figure also reveals that the efficiency of the period estimation is even higher, reaching  $\sim 90\%$ . It is important

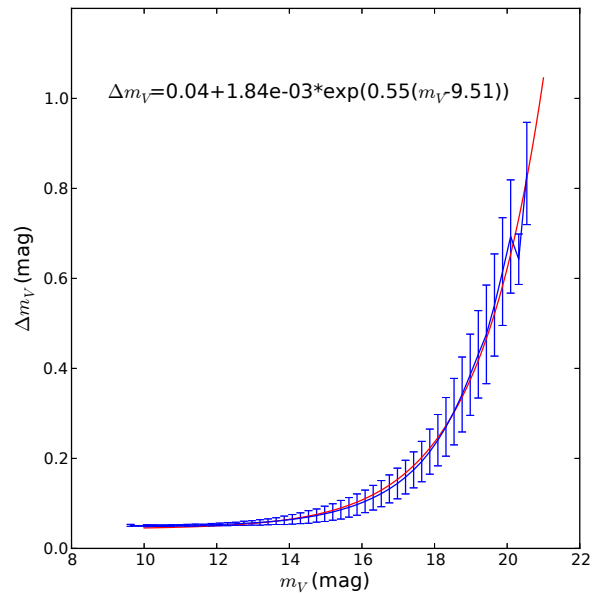


**Figure 7.** Photometric error as a function of apparent magnitude for the SSS survey. Red line represents the exponential model fit to the mean error in each magnitude bin. This is the model used to produce synthetic lightcurves as described in Section 4.3.

to mention that the APS was set to have the cleanest sample possible in a fully automatic mode which explains why the efficiency drops down at the faint end. This is, of course, unavoidable since at these magnitudes the photometric error becomes comparable to the pulse amplitudes of RRab stars, making it difficult for a fully automated procedure to identify correctly the exact type of variability. Nevertheless, as part of the output of the program, the information on the rejected stars is recorded, so that the faint RRab discarded by our search algorithm can be recovered in the future.

The analysis described above concerns only the efficiency of the period determination and the RRab classification. The actual completeness of our sample, i.e. the amount of stars expected to be recovered versus the actual number of stars measured, needs to take into account the variability and the periodicity checks described in Section 2. An example of an empirical approach to check the completeness of the RRab sample can be found in Drake et al. (2013a), which reports an efficiency of  $\sim 70\%$  for the RRab sample found by the CSS. Since both the CSS and the SSS performed the same steps to classify RRab, this could serve as an adequate estimate of the overall completeness of the SSS RRab sample presented in this paper. In fact, we have verified this statement by counting all stars that lie in the SSS footprint and are recorded as RRab in the VSX catalog (Watson 2006). There are 1919 RRab in the VSX of which we identify 1321, resulting in a completeness level of  $\sim 69\%$ . If we now remove detections along the borders of the survey, where objects can be spuriously included even if they were not observed sufficiently often by the SSS, we identify 1075 out of 1521 stars, raising the completeness to  $\sim 71\%$ . These tests illustrate that our efficiency is a strong function of the temporal sampling, increasing in the areas of the sky visited by the SSS more frequently. For example, if we fur-

<sup>1</sup> Note that Table 2 includes the lightcurve information necessary to derive photometric metallicities in different scales



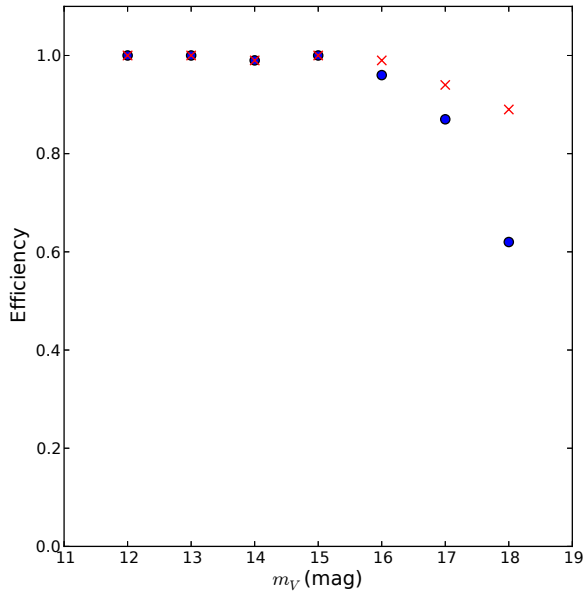


**Figure 8.** Reliability of period (red crosses) and RRAb (filled blue circles) selection as a function of magnitude. Each datapoint gives the fraction of stars recovered from the synthetic sample as a function of the apparent magnitude.

ther limit the region of interest to  $190 < \alpha(\text{deg}) < 235$  and  $-23 < \delta(\text{deg}) < -35$ , i.e. the area sampled the densest by the SSS, we detect 84% of the RRAb's in the VSX database. While this is encouraging, completeness estimates based on a comparison between our detections and the VSX entries should be taken with due caution, as the VSX catalog is highly inhomogeneous and has a much brighter cutoff with respect to SSS. Most importantly, we note that the VSX catalog is highly incomplete in the Southern hemisphere, as it contains less than 10% of the total number of RRAb's we have discovered.

## 5 GALACTIC STELLAR HALO WITH NEW RR LYRAE

From the original sample of 18,288 variable star candidates with periods between 0.3 and 4 days, we have selected 10,540 RRAb stars, of which 8,869 correspond to new discoveries, 231 correspond to stars previously reported as RRAb by Drake et al. (2013a), and the remaining 1,440 correspond to stars previously available in the literature. Figure 9 displays several examples of light curves for the RR Lyrae identified in our search. Figure 10 presents the distribution of RRAb on the sky, using discoveries from all three Catalina surveys. For all stars in the SSS we provide metallicity, distance, Galactic position, and lightcurve shape information (through the AFD parameters). Table 2 shows an extract from our RRAb catalog.

Figure 11 presents the distribution of the discovered RRAb stars across the period-amplitude diagram (also known as Bailey diagram). As shown previously by Drake et al. (2013a), amplitudes of RRAb stars in our sample are systematically reduced by 0.15 mag when compared

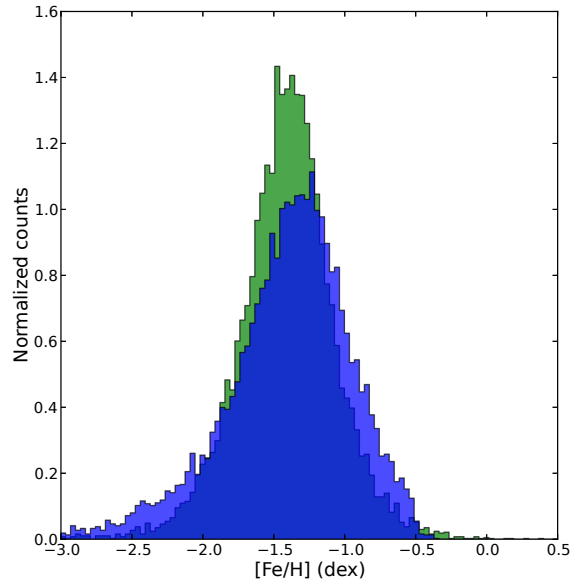


**Figure 12.** Metallicity distribution of the SSS RRAb stars according to Jurcsik & Kovács (1996) (green) and Nemec et al. (2013) (blue) relations. The histograms are normalized to the same area. The green histogram can be described by a Gaussian distribution with a peak at  $[\text{Fe}/\text{H}] = -1.40$  dex and a dispersion of 0.20 dex, whereas the blue histogram shows the presence of a metal-poor tail and an excess of stars in the range  $-1.0 < [\text{Fe}/\text{H}] < -0.5$ . The existence of these differences in the metallicity estimated based on the RRAb lightcurve shape is in agreement with previous studies highlighting that Jurcsik & Kovács (1996) metallicities are typically higher than expected in the metal-poor regime. Also note that a new discrepancy appears in the metal-rich regime, where the Jurcsik & Kovács (1996) relation seems to underestimate the  $[\text{Fe}/\text{H}]$  values.

to the typical RRAb amplitudes. As a result, we provide a correction to the amplitudes to account for this effect. The diagram shows the Zorotovic et al. (2010) Oosterhoff type-I (OoI) and Oosterhoff type-II (OoII) lines, and the period shift with respect to the OoI line is shown on the right panel. This suggests that our data is composed of stars belonging to both OoI and OoII types, with the OoI population clearly being the dominant one. As in Drake et al. (2013a), we too find that the distribution is bimodal, with relatively few stars present between the canonical OoI and OoII loci.

### 5.1 Halo Metallicity

Carretta et al. (2009) presents a new homogeneous metallicity scale, which is calibrated using high resolution spectra from UVES. It also provides transformations from the most used metallicity scales. The fact that this scale has been calibrated using a large sample of GC red giants with homogeneously measured metal abundances from high resolution spectroscopy, makes this scale a good candidate to homogenize the metallicity measurements for RR Lyrae. In this sense, we transform all our metallicities to the UVES metallicity scale provided by Carretta et al. (2009). The total number of RRAb stars with metallicities in our sample is 10,540. This number is reduced slightly after the removal

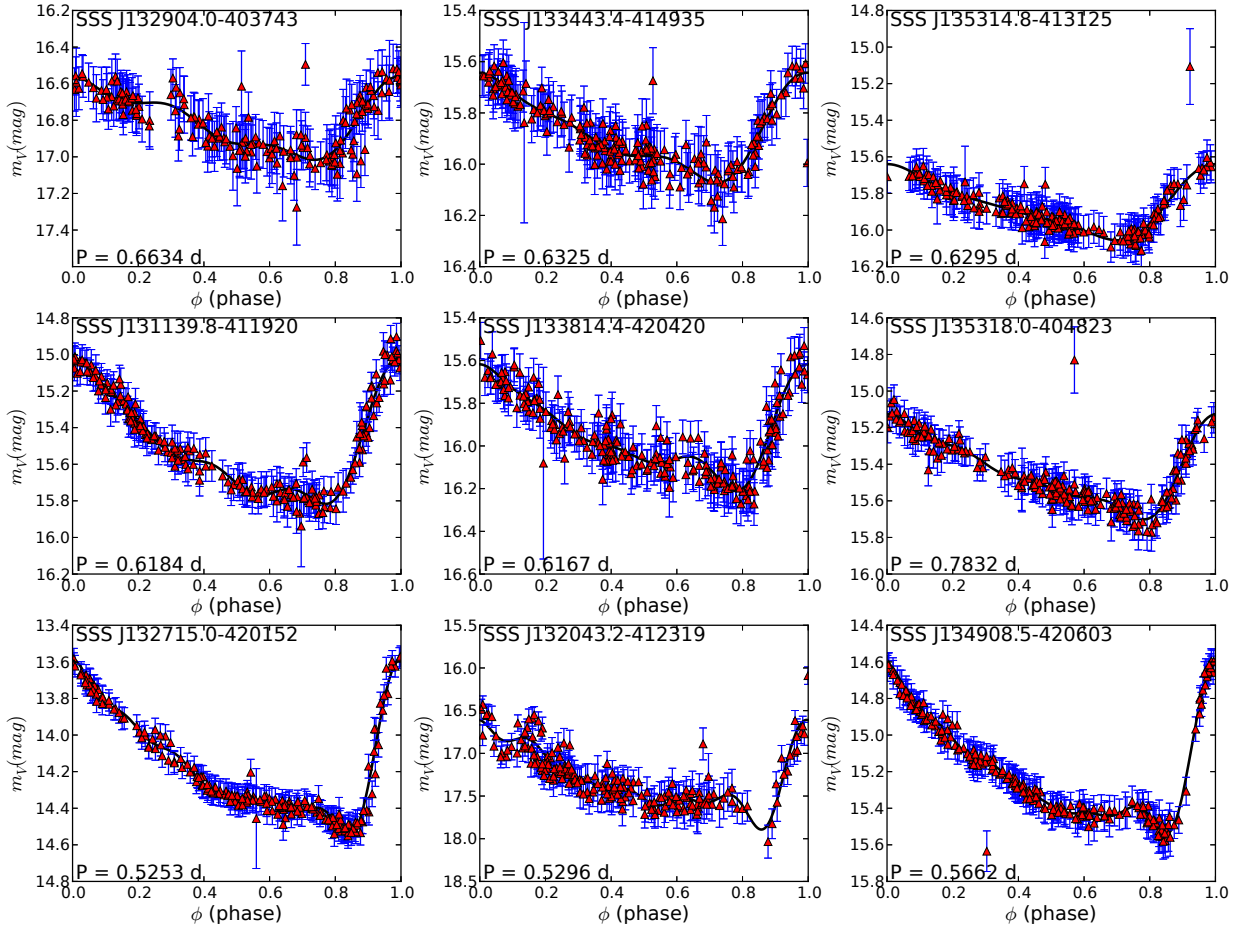


**Figure 9.** Examples of RRab lightcurves. From top to bottom, lightcurves of sample RRab variables that require 3 (top), 4 (middle), and 6 (bottom) Fourier harmonics in the model fit. The ID and the period in days are given for each star.

**Table 2.** RRab sample selection

ID	RA (deg)	Dec (deg)	$m_V$ (mag)	Period (days)	Amp (mag)	$n_{obs}$	$d_H$ (Kpc)	[Fe/H] (dex)	E(B-V)	$D_m$	$\phi_{31}$ (rad)	ID <sub>alt</sub>
SSS_J055136.9-143214	87.90386	-14.5371	12.87	0.51901	0.77	82	2.24	-1.38	0.176	5.3	4.97	BF_Lep
SSS_J085855.1-151229	134.72958	-15.20811	15.8	0.58286	0.75	95	10.32	-1.87	0.047	42.7	4.29	...
SSS_J090949.5-153559	137.45624	-15.59973	12.02	0.50775	1.05	119	1.75	-1.16	0.082	5.6	5.38	XX_Hya
SSS_J091750.5-151433	139.46041	-15.24257	12.9	0.66385	0.38	124	3.05	-2.59	0.055	85.8	5.47	VSX_J091750.5-151433
SSS_J092942.0-154231	142.42515	-15.70864	15.61	0.49154	1.14	126	8.48	-1.46	0.0686	5.5	4.99	...
SSS_J093650.9-150241	144.21208	-15.04463	17.57	0.52288	1.06	115	23.52	-1.46	0.069	12.7	6.18	...
SSS_J093543.0-150150	143.92933	-15.03052	15.1	0.64336	0.26	115	6.96	-1.27	0.076	131.7	5.49	...
SSS_J094138.1-155627	145.40875	-15.94082	16.54	0.50207	1.08	117	9.58	-1.78	0.0681	49.7	5.5	CSS_J094138.1-155626
SSS_J095250.9-143253	148.21227	-14.54792	16.31	0.5016	1.19	118	12.46	-1.31	0.0574	4.5	4.5	CSS_J095251.0-143253
SSS_J094959.6-141035	147.4988	-14.17705	15.89	0.57123	0.77	114	10.85	-1.56	0.052	6.9	4.66	CSS_J094959.6-141035
SSS_J100008.3-153936	150.0344	-15.66008	17.08	0.49428	1.15	126	16.16	-1.54	0.0506	12.3	5.66	...

Notes: Column 1 gives the SSS id; Column 2 and 3 give the right ascension and declination; Column 4 gives the average magnitude, as given by the AFD; Column 5 gives the period; Column 6 gives the amplitude of the lightcurve, as given by the AFD; Column 7 gives the number of photometric observations; Column 8 gives the distance to the Sun, in kpc; Column 9 gives the metallicity, as given by eq. 7 and transformed to the UVES scales with eq. 9; Column 10 gives the reddening, as given by Schlegel et al. (1998); Column 11 give the value of  $D_m$ , which gives us an estimate of the reliability of the photometric metallicities according to Jurcsik & Kovács (1996); Column 12 gives the value of  $\phi_{31}$ ; Column 13 gives the id for sources that were previously known. This table is available in its entirety in a machine-readable form in the online journal. A portion is shown here for guidance regarding its form and content.

of obvious outliers, that is, the stars whose metallicities fall outside the range  $-3.0 < [\text{Fe}/\text{H}] < 0.5$ . This leaves a total of 10,369 stars with photometric metallicities, an ample resource to probe the properties of the Galactic halo out to 40 kpc. Figure 12 shows two metallicity distributions, one

found using the Jurcsik & Kovács (1996) relation (green) and the results of the alternative  $[\text{Fe}/\text{H}]$  determination with formulae from Nemec et al. (2013) (blue). As the error propagation cannot presently be implemented for the latter, in order to compare the two distributions, we have to assign

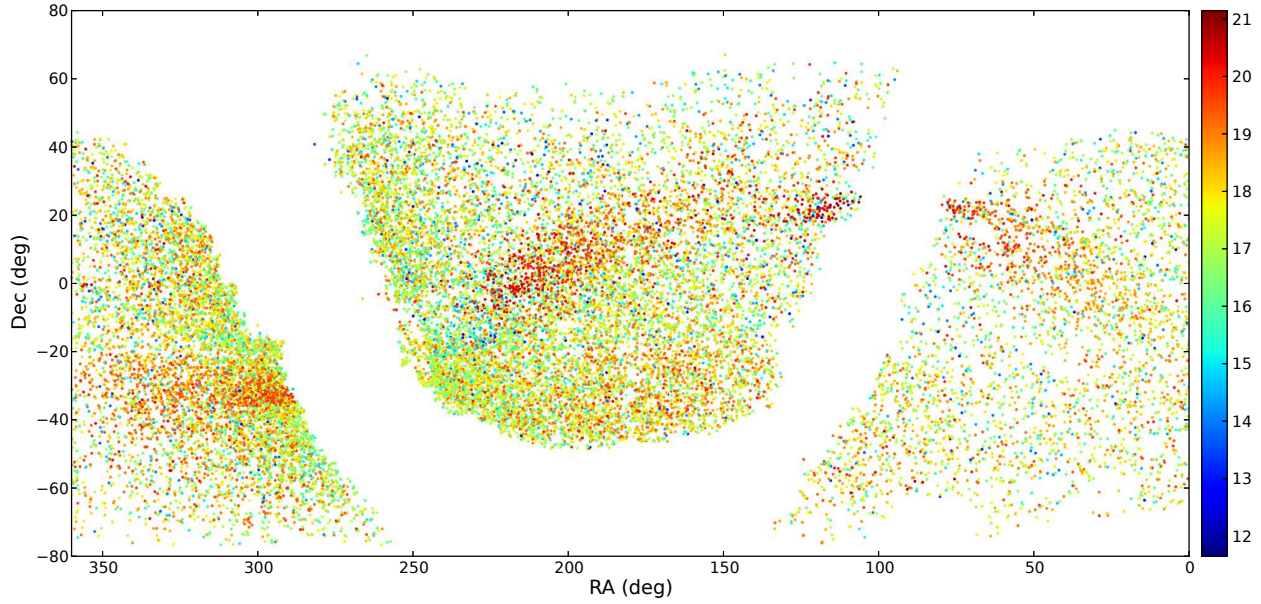


**Figure 10.** Distribution of all RRab stars discovered in the three Catalina surveys in equatorial coordinates. The color represents the magnitude of each star, following the color code on the right. The obvious stream-like pattern running across the Figure is the Sagittarius tidal tail system. The new RRab found in the SSS lie below  $\text{Dec} = -20^\circ$ . These trace the beginning of the trailing arm starting at  $\text{RA} \sim 290^\circ$  and  $\text{Dec} \sim -30^\circ$ .

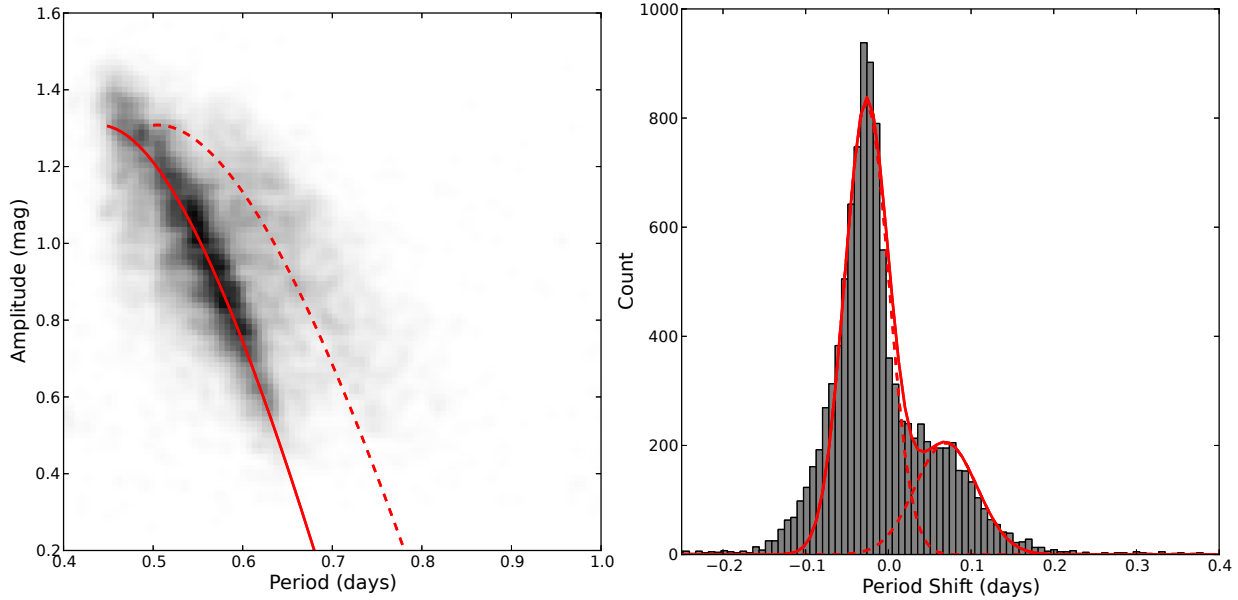


**Figure 11.** *Left:* Period-amplitude diagram of the selected RRab stars. For reference, lines corresponding to the OoI (solid) and OoII (dashed) objects based on Equation 11 of Zorotovic et al. (2010) are overlaid. *Right:* Histogram of the period difference (at fixed amplitude) between the detected RRab's and the OoI reference line. The red lines shows a two-Gaussian fit to the histogram. This distribution is similar to what is shown in Drake et al. (2013a) for the RRab identified in the Northern hemisphere. Similarly, our result suggests an overall bi-modal population composed by both OoI and OoII RRab stars, with the OoI sub-sample being notably larger compared to the OoII one. The excess of stars observed in low-period-shift regime may be caused by RR Lyraes that present the Blazhko effect.

uncertainties found using the Jurcsik & Kovács (1996) relation to  $[\text{Fe}/\text{H}]$  values obtained according to Nemec et al. (2013). For the Jurcsik & Kovács (1996) metallicities, the histogram has a shape that can be well approximated by a Gaussian with a mean metallicity of  $[\text{Fe}/\text{H}] = -1.41$  dex and a standard deviation of 0.27 dex. Note that if we limit the sample to the stars with reliable metallicity estimates in accordance with the criteria from Jurcsik & Kovács (i.e., with values of  $D_m < 5$ ; this gives a total of 1,880 stars), the mean of the distribution remains the same at  $[\text{Fe}/\text{H}] = -1.40$  dex, but the dispersion shrinks slightly, to 0.20 dex. This result appears to be in good agreement with independent, spectroscopic analyses of the halo RR Lyrae and blue horizontal-branch stars (e.g., Kinman et al. 2000; Drake et al. 2013a, and references therein). Small differences, such as the presence of a metal-rich tail and/or lack of an extremely metal-poor tail ( $[\text{Fe}/\text{H}] \ll -2$  dex), could be due to small systematic differences in the metallicity scale adopted, as well as the lack of very metal-poor calibrators in the Jurcsik & Kovács (1996) sample. Naturally, the RR Lyrae metallicity distribution cannot be directly compared with the one derived using other stellar tracers, be it main-sequence stars (e.g., An et al. 2012, and references therein) or giants. This is because the formation mechanism of RR Lyrae stars is far from uniform as a function of metallicity: it peaks around  $[\text{Fe}/\text{H}] \approx -1.5$  (e.g., Catelan & de Freitas Pacheco 1993; Layden 1995; Kinman et al. 2009). Note that the distribution of the Nemec et al. (2013) metallicities mostly agrees with that built using the Jurcsik & Kovács (1996) prescription, except for the appearance of a metal-poor tail, confirming that the Jurcsik & Kovács (1996) method does indeed overestimate the metallicities at the very low end. Interestingly, we also find an excess of stars in the metal-rich end, where it seems that the Jurcsik & Kovács (1996) method is underestimating the  $[\text{Fe}/\text{H}]$  values.

Let us study the spatial variations of the R Rab metallicity in the halo. For the analysis described below, to obtain reliable space coverage, we choose to include stars with  $D_m > 5$  as their metallicity distribution does not look significantly different from that of the stars with reliable  $[\text{Fe}/\text{H}]$ . Figure 13 shows the mean R Rab metallicity as a function of Galactic cylindrical radius,  $r_{xy} = \sqrt{x^2 + y^2}$  (top panel), and as a function of the distance from the Galactic plane  $z$  (bottom panel). The bin size for each of the x axes is chosen adaptively so that there are 500 stars in each bin. The figure gives the mean and its error for each bin, for both the Nemec et al. (2013) metallicities (black), as well as the Jurcsik & Kovács (1996) metallicities (red). Note that while the  $[\text{Fe}/\text{H}]$  spread in each bin is large ( $\sigma \sim 0.35$  dex), the uncertainty of the mean, due to moderate uncertainties on individual metallicities and large number of stars in our sample, remains small ( $\sim 0.02$  dex).

The top panel of Figure 13 reveals a small but nonetheless very clear negative metallicity gradient both in Galactocentric distance and in distance from the Galactic plane, regardless of the  $[\text{Fe}/\text{H}]$  recipe used. Note that as a function of Galactocentric radius, the mean metallicity starts to drop at  $\sim 7$  kpc, having remained approximately constant in the first few kpc. This is in good agreement with previous studies of the metallicity gradient (e.g., Szczygiel et al. 2009; Kinemuchi et al. 2006), where the authors claim a lack of evidence for a metallicity gradient in the first  $\sim 10$  kpc. How-

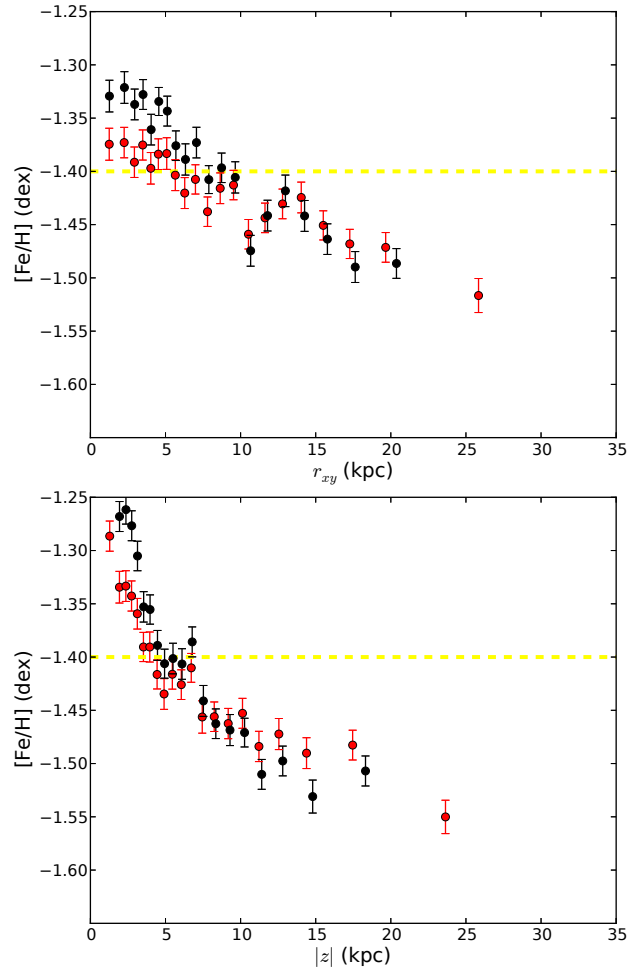


**Figure 13.** Spatial variations of the R Rab metallicity in the SSS. In both panels, the bin-size along the x-axis is varied to make sure that there are 500 stars in each bin. Red (black) symbols show average R Rab metallicities obtained with the Jurcsik & Kovács (1996) (Nemec et al. (2013)) relation. *Top:* Mean metallicity (filled circles) and the associated error for bins of Galactocentric cylindrical radius. Note a constant metallicity in the first 4 to 5 kpc from the Galactic centre. This is followed by a modest but statistically significant negative metallicity gradient for R Rab's with  $7 < r_{xy}(\text{kpc}) < 25$ . *Bottom:* Mean metallicity (filled circles) and the associated error for bins of distance above Galactic plane  $|z|$ . Note a steep  $[\text{Fe}/\text{H}]$  gradient in the first 5 kpc, followed by a much shallower slope for stars with  $7 < |z|(\text{kpc}) < 25$ . It can also be seen that the Nemec et al. (2013) relation indicates a higher concentration of more metal-rich stars near the disk.

ever, as Figure 13 makes apparent, this behaviour changes at larger distances from the Galactic center. Out to  $r_{xy} \sim 10$  kpc, the Nemec et al. (2013) estimate of metallicity is consistently higher (by approximately one standard deviation) as compared to that of Jurcsik & Kovács (1996), which suggests that the excess of stars with  $[\text{Fe}/\text{H}] > -1$  according to Nemec et al. (2013) (as seen in Figure 12) is preferentially located within the Solar radius. Moreover, as the lower panel illustrates, these stars live very close to the Galactic disk. This panel also reveals an obvious dependence of the mean R Rab metallicity on  $|z|$  as well as a concentration of high metallicity R Rab in the first few kpc, which is consistent

with the hypothesis that the high metallicity R Rab's belong primarily to the Milky Way's disk (Kinemuchi et al. 2006). We also note the possible detection of a small bump in the radial profile of the mean R Rab metallicity at  $r_{xy} \sim 13$  kpc. We have checked the possibility that the bump is due to presence of the Sagittarius stream in our dataset. However, the removal of the likely Sgr members has no noticeable affect on this feature.

## 5.2 A sweep for obvious halo sub-structure

In this section we carry out a simple overdensity search using the discovered R Rab as tracers. Our method takes advantage of the available 3D information and picks up the most obvious (largely, previously unknown) overdensity candidates in the southern celestial hemisphere. To find significant enhancements in R Rab density, we calculate the local stellar density around every star and compare it to the prediction of a smooth stellar halo model. We keep track of those positions where the observed number of stars is substantially higher than the expected number, as given by the model. The coordinates as well as some of the structural properties of the detected candidates are given in Table 3.

The observed density is calculated using the N-th neighbor method, originally proposed by Dressler (1980). At each trial position, this algorithm takes the distance to the N-th nearest star as the radius of the sphere containing N stars. Then the number density at the selected position is simply given by:

$$\rho_t = \frac{N}{\frac{4}{3}\pi d_N^3}, \quad (14)$$

where  $d_N$  is the distance to the N-th star from the selected position. The local density estimate is then compared to the prediction of the halo model, in particular, we use the model proposed by Sesar et al. (2010). This is a flattened power-law as defined by:

$$\rho_m = \rho_0 \left[ \frac{R_\odot}{\sqrt{x^2 + y^2 + (z/q_H)^2}} \right]^{n_H}, \quad (15)$$

where  $\rho_0 = 4.2 \text{ kpc}^{-3}$  is the number density of R Rab stars at  $R_\odot = 8.0$  kpc (Vivas & Zinn 2006),  $q_H = 0.64$  stipulates the oblateness of the halo (Sesar et al. 2010),  $n_H = 2.77$  is the power-law index (Jurić et al. 2008), and  $x$ ,  $y$ , and  $z$  are Cartesian coordinates in the Galacto-centric system. In order to select the stars associated with each overdensity candidate, we determine the extent of the sub-structure by calculating 3D density contours around its peak. The outermost contour is set to a density 0.5 times smaller than the peak density of the candidate. The significance is then obtained by assuming the Poissonian statistics for the incidence of the sub-structure member stars.

By applying the method described above to our sample of SSS RR Lyrae, we have discovered several interesting candidates; in particular, there are 12 possible objects each with significance greater than  $3 \sigma$ . Table 3 summarizes the properties of all candidates with significance greater than  $2 \sigma$ . This table includes information regarding the shape of the candidate by listing its extent in RA and Dec, as well

as its heliocentric distance. To illustrate the distribution of the sub-structure candidates in the Galaxy, we have plotted their approximate shapes in equatorial coordinates in Figure 14. Here, the color of each polygon represents the mean heliocentric distance of the stars bounded by the region. All SSS variable candidates are plotted in greyscale in the background of the figure, to show the survey's limits. Please bear in mind that the objects that are located closer will naturally appear bigger in this figure. Additionally, it is also worth noting that the second most prominent candidate, Hya 1, situated very close to the Galactic center, has a very large size. This may simply be caused by the algorithm selecting too big an area around a genuine overdensity close to the MW center (note that the significance, in this specific case, is  $\sim 9 \sigma$ ). This could be due to the model (see equation 15) producing an underestimate of the true number of R Rab stars in this region of the Galaxy. Note that the same may apply to Col 1 and Tel 1 which are close to the MW disk. In their case, its significance might also be inflated due to a poor estimation of the amount of background stars by the model. Conversely, some of the candidates in the range  $130 \text{ deg} \lesssim \text{RA} \lesssim 250 \text{ deg}$  could plausibly be related to the VOD. To confirm the nature of these overdensity candidates, deep wide-area imaging and spectroscopic data would be necessary.

## 5.3 Sagittarius stream in SSS data

The most prominent of the sub-structure candidates detected by the algorithm described above has a striking significance of  $> 15 \sigma$ , and an impressive total of 327 R Rab stars associated with it. The mean position of the constituent stars is at  $\alpha = 307.53^\circ$ ,  $\delta = -32.132^\circ$ , at a distance of  $\sim 24$  kpc from the Sun and  $\sim 18$  kpc from the Galactic center. The overdensity has an elongated, stream-like shape, with a length of about 17 kpc and a width of about 6 kpc. Given its 3D position, it is almost certainly a part of the Sagittarius stream. Therefore, its designated name is Sgr 1.

To visualize the overdensity and to highlight its connection to the Sagittarius dwarf, Figure 15 presents the density distribution of all R Rab stars detected by CRTS in the plane spanned by right ascension and heliocentric distance, after subtracting a model stellar halo. The R Rab overdensities are colored according to the logarithm of the ratio of the observed and model density,  $\log(\rho_{\text{obs}}/\rho_{\text{mod}})$ . Here  $\rho_{\text{obs}}$  is the observed local density defined by equation 14, and  $\rho_{\text{mod}}$  is the model density defined by equation 15. In this plotting scheme, the color is saturated at 1 and -1, and the size of the points is scaled to represent the logarithm of the ratio of the densities in order to improve the visualization.

According to previous studies (e.g., Majewski et al. 2003; Belokurov et al. 2014b), Sgr 1, the overdensity picked up in the South in the SSS dataset, is a portion of the Sgr trailing stream. Correspondingly, the structure in the north, visible in the CSS data, is the leading tidal tail. The portion of the trailing stream found using the SSS data is located at approximately  $\alpha \sim 300^\circ$ ,  $D_h \sim 30$  kpc. It is curious to see that along the line of sight, the debris seem to spray over a large range of distances. At the moment, it is difficult to conclude with certainty whether this apparent clutter is a genuine sub-structure in the Sgr trailing tail, or actually bits of other, overlapping tidal streams like, for example, Cetus



**Table 3.** Overdensity Candidates in the Galactic Halo

ID (1)	ID (2)	S ( $\sigma$ )	RA (deg)	Dec (deg)	$n_{RRL}$	$m_V$ (mag)	$m_{V,min}$ (mag)	$m_{V,max}$ (mag)	$\Delta D$ (kpc)	$\Delta \alpha \cos \delta$ (deg)	$\Delta \delta$ (deg)
Sgr 1	SSSOc_J203007-320757	15.79	307.53	-32.13	327	17.71	16.71	18.38	13.0	48.6	20.8
Hya 1	SSSOc_J145754-283033	9.10	224.48	-28.52	179	14.03	12.56	15.22	4.2	70.9	29.6
Cen 1	SSSOc_J130248-320118	4.74	195.70	-32.02	46	15.63	15.30	16.05	2.4	15.3	20.5
Cen 2	SSSOc_J112907-394650	4.41	172.28	-39.78	35	16.72	16.32	17.12	4.4	17.8	13.0
Hya 2	SSSOc_J100540-245134	4.15	151.42	-24.86	29	15.61	15.27	15.97	2.7	19.0	17.9
Sgr 2	SSSOc_J202727-372132	4.06	306.87	-37.36	36	13.67	12.83	14.18	2.0	23.0	14.6
Hya 3	SSSOc_J111948-252007	3.84	169.95	-25.34	21	16.75	16.53	17.11	3.8	9.6	7.2
Hya 4	SSSOc_J124106-281257	3.84	190.28	-28.22	27	16.18	15.98	16.61	2.9	11.3	8.3
Tel 1	SSSOc_J184232-553460	3.46	280.64	-55.58	21	14.09	13.73	14.48	1.1	8.0	16.2
Cen 3	SSSOc_J114153-393448	3.33	175.47	-39.58	20	15.92	15.60	16.37	3.3	8.3	7.7
Cen 4	SSSOc_J124936-391616	3.20	192.40	-39.27	16	16.12	15.98	16.31	1.3	9.4	6.3
Ant 1	SSSOc_J101002-282309	3.03	152.51	-28.39	24	14.95	14.68	15.22	2.1	23.5	15.3
Crv 1	SSSOc_J124414-155910	2.99	191.06	-15.99	15	16.00	15.71	16.31	2.6	9.1	5.6
Tel 2	SSSOc_J194146-495134	2.82	295.44	-49.86	17	12.39	11.87	12.95	0.9	10.0	34.1
Sgr 3	SSSOc_J193812-382955	2.76	294.55	-38.50	17	15.10	14.77	15.34	0.8	6.3	4.4
Cen 5	SSSOc_J133306-331937	2.75	203.28	-33.33	18	14.41	14.21	14.66	0.8	9.1	13.0
Lib 1	SSSOc_J153446-265727	2.75	233.69	-26.95	22	15.01	14.62	15.38	1.2	11.3	7.5
Ant 2	SSSOc_J101614-331524	2.56	154.06	-33.26	13	16.94	16.76	17.05	1.1	5.7	7.7
Cen 1	SSSOc_J140450-143546	2.50	211.21	-41.60	13	14.78	14.57	15.03	0.7	5.1	5.7
Hya 5	SSSOc_J103240-212215	2.50	158.17	-21.37	11	17.00	16.81	17.16	1.9	7.6	7.0
Cap 1	SSSOc_J204404-230214	2.46	311.02	-23.04	10	14.68	14.59	14.80	0.5	5.3	3.7
Cen 7	SSSOc_J115216-365325	2.45	178.07	-36.89	7	14.28	14.09	14.42	0.4	6.7	5.4
Lep 1	SSSOc_J061057-254429	2.44	92.74	-25.74	9	15.59	15.41	15.79	1.5	13.2	5.6
Col 1	SSSOc_J060924-321527	2.37	92.35	-32.26	12	14.89	14.44	15.39	2.5	12.3	18.6
Sgr 4	SSSOc_J202138-435633	2.36	305.41	-43.94	9	16.72	16.60	16.89	1.6	2.9	5.4
Sc1 1	SSSOc_J011639-313912	2.18	19.16	-31.65	9	15.72	15.46	15.95	1.9	15.0	6.7
Crt 1	SSSOc_J111824-181426	2.17	169.60	-18.24	10	15.64	15.44	15.81	1.1	8.2	6.0

Notes: Column 1 gives a reference id; Column 2 gives the Overdensity id; Column 3 gives the significance in standard deviations; Columns 4 and 5 give the mean right ascension and declination of the stars of the overdensity; Column 6 gives the number of stars associated with the overdensity; Column 7 gives the mean magnitude of the stars of the overdensity; Columns 8 and 9 give the minimum and maximum magnitude of the stars of the overdensity, respectively; Column 10 gives the overdensity's extension along the line of sight, in kpc; Columns 11 and 12 give the extension in equatorial coordinates.

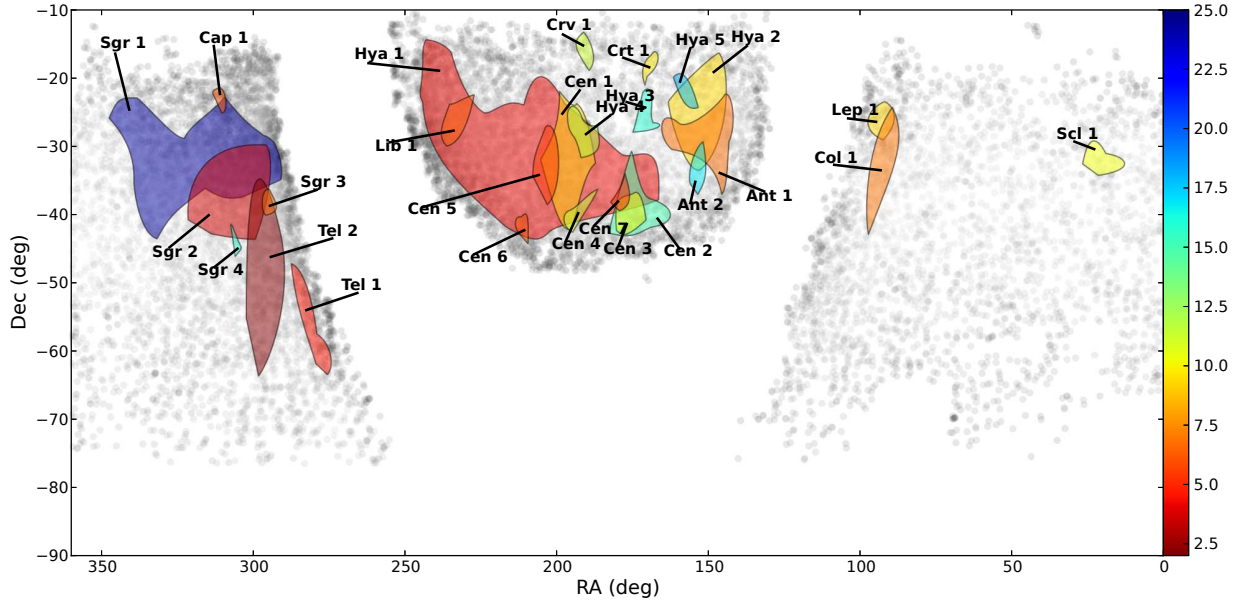


**Figure 14.** Locations and shapes of the SSS RRAb overdensity candidates as presented in Table 3. The shapes are labeled according to the reference ID given in Column 1 of the table, and the color of each shape reflects the mean heliocentric distance to the constituent stars (see color-bar for reference in kpc). The background greyscale distribution shows all SSS variable candidates; the shades of grey are coded according to the logarithm of the number of observations.

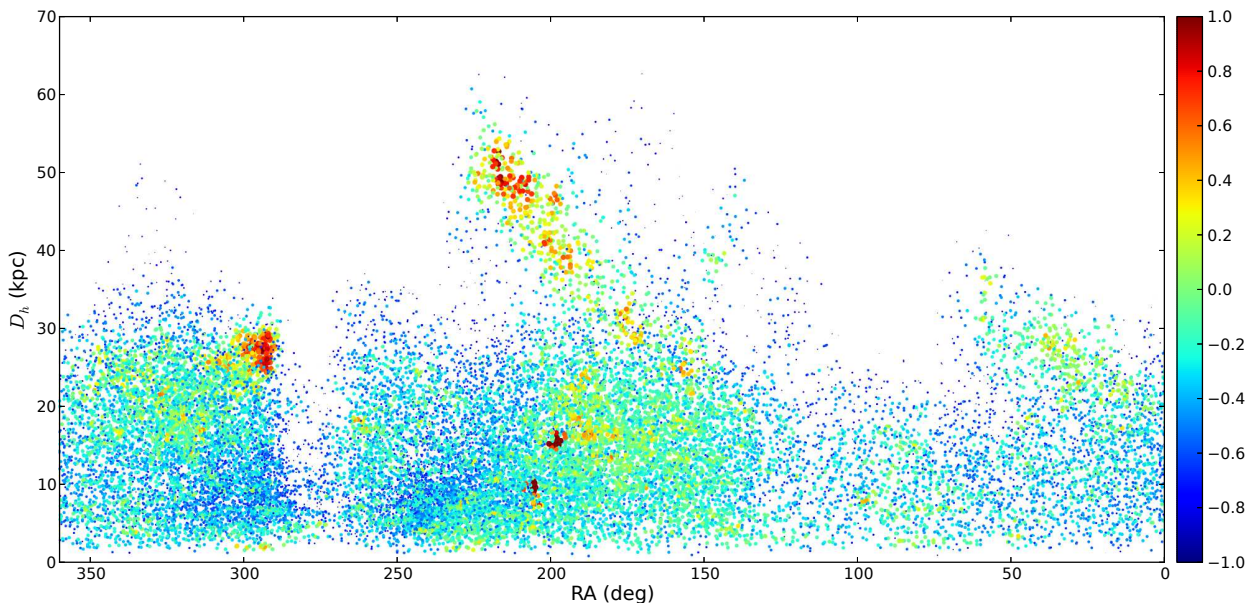


**Figure 15.** Map of RRab overdensity along the line-of-sight. This shows the density distribution of all Catalina RRab stars in the space spanned by RA and heliocentric distance,  $D_h$ , after the subtraction of a stellar halo model. The most prominent feature in the Figure is the Sagittarius stream. The color coding (see scale on the right) gives the logarithm of the ratio of the observed to the expected stellar density. To improve visualization, we saturate the color at  $\pm 1$  and scale the size of the points according to the color. The position of the Sgr 1 candidate substructure is at  $\alpha \sim 300^\circ$ ,  $D_h \sim 30$ . It extends to  $\alpha \sim 360^\circ$ , where the distance gradient changes sign as the trailing tail starts to move away from the Sun until it disappears from the view at  $\alpha \sim 60^\circ$ . In the north, the range of  $220^\circ < \alpha < 150^\circ$  is dominated by the Sagittarius leading arm debris coming down from its apo-centre at around 55 kpc near  $\alpha \sim 220^\circ$  to  $\sim 20$  kpc at  $\alpha \sim 150^\circ$ . At lower distances, a more diffuse, cloud-like feature is the VOD. The two dense regions at  $\alpha \sim 200^\circ$  correspond to M3 (NGC 5272), at  $\sim 10$  kpc, and M53 (NGC 5024), at  $\sim 15.5$  kpc.

(see Koposov et al. 2012). Further away from the progenitor, there is an obvious extension of the trailing debris to larger distances at  $0^\circ < \alpha < 70^\circ$ . The leading tail runs from  $(\alpha, D_h) = (230^\circ, 50 \text{ kpc})$  to  $(\alpha, D_h) = (150^\circ, 20 \text{ kpc})$ . Additionally, the Figure shows a clump of stars at  $\alpha \sim 150$  with distances between 30 and 50 kpc. This has already been reported as candidate D in Drake et al. (2013b), and, given its position and distance, is likely associated with the Orphan stream (see e.g. Belokurov et al. 2007b; Sesar et al. 2013).

Finally, Figure 16 displays the distribution of the RRab stars around the Sagittarius plane in equatorial coordinates. Adopting the Majewski et al. (2003) Cartesian coordinate system, stars that are more than 2.5 kpc away from the Sagittarius plane are removed. This highlights the shape of the two main arms of the Sagittarius stream, leading in the north, and trailing in the South. Sgr 1, the overdensity detected in this analysis (see Table 3), can be seen at Dec  $\sim -30^\circ$ ; note how this feature extends to higher RA, from  $\sim 300^\circ$  to  $\sim 360^\circ$ , as also seen in Figure 14.

## 6 CONCLUSIONS

With the aim to find and classify RR Lyrae, we have carried out a systematic study of a large variable star database covering most of the Southern celestial hemisphere ( $-75^\circ \leq \delta \leq -22^\circ$ ). Using the data from the extension of the Catalina Sky Surveys, the SSS, we have discovered more than 10,500 ab-type RR Lyrae,  $\sim 90\%$  of which are new. Our sample cov-

ers a range in apparent brightness from  $10.5 \leq V \leq 19.3$ , corresponding to heliocentric distances from  $\sim 1$  to  $\sim 50$  kpc. The RRab stars have been found using fully automated procedures that could be applied to any other variability survey. These algorithms boast, depending on the quality of the photometry, a completeness of RRab classification greater than 60% at  $V = 18$ , and an efficiency of the period estimation  $> 90\%$ . The software leaves the possibility of manual classification of the faintest stars, including other types of periodic variables, using the lightcurve shape and period information recorded.

We take advantage of the metallicity information available as a result of the RRab lightcurve shape analysis to study the abundance patterns in the Galactic stellar halo. The  $[\text{Fe}/\text{H}]$  distribution appears roughly Gaussian with a mean metallicity of  $[\text{Fe}/\text{H}] = -1.4$  dex and a dispersion of 0.3 dex, which is consistent with previous work. A comparison between the Jurcsik & Kovács (1996) and the Nemec et al. (2013) period- $\phi_{31}$ -metallicity relation reveals clear differences at both the metal-poor end, where the presence of a significant tail is highlighted, as well as in the metal-rich range, where there seems to be an excess of stars with metallicities between -1.0 and -0.5 dex, according to estimates based on the Nemec et al. (2013) relation.

A spatial study of the metallicity gradients reveals a modest but statistically significant  $[\text{Fe}/\text{H}]$  trend with both the Galactocentric distance and the height above the disc plane. We confirm that the RRab stars with lower metallicities are more common further away from the Galactic

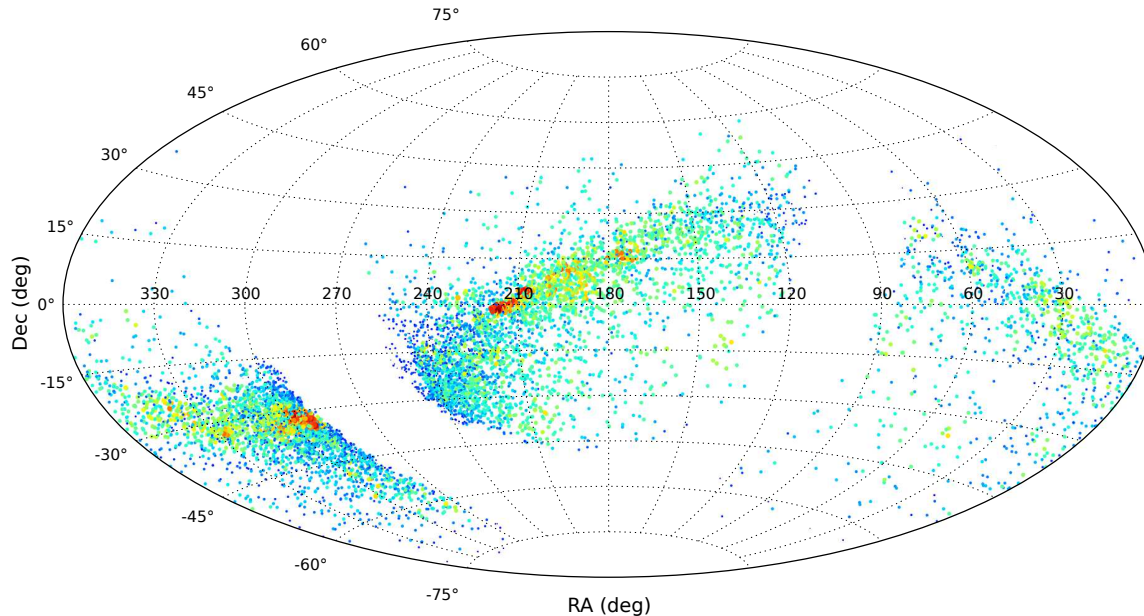


**Figure 16.** Distribution of RRab stars near the Sgr orbital plane in equatorial coordinates. This shows the Aitoff projection of the distribution of all stars with  $|Z_{sgr}| < 2.5$  kpc. The color gives, according to the same scale used in Figure 15, the ratio of the observed local density and the expected local density according to Equation 15. Note that the size of the points also scales with the density ratio. The scale and the continuity of the Sgr stream system is obvious, with the leading debris dominating the picture above the celestial equator and the trailing tail visible mostly in the south.

center and the Galactic plane in general. The radial gradient appears approximately flat in the first  $\sim 7$  kpc but starts to steepen at larger distances. When compared to the  $[\text{Fe}/\text{H}]$  behaviour with  $z$ , this flattening is not present in the first few kpc. On the contrary, an accumulation of high-metallicity RRab stars in the first  $\sim 2$  kpc is apparent, which is consistent with the hypothesis that high-metallicity RRab stars belong primarily to the Galactic disc population. This low- $z$ , high-metallicity concentration is even more pronounced when the Nemec et al. (2013)  $[\text{Fe}/\text{H}]$  estimates are considered.

A preliminary analysis of possible halo sub-structure using the RRab detected in the Southern hemisphere shows the presence of several interesting overdensities. The locations and the structural properties of the most significant twenty-seven of these are given in tabular format. We have presented the properties of the most obvious of the overdensity candidates discovered in our sample, the one with the significance  $> 15\sigma$  and some  $\sim 330$  RRab associated. Given its shape, spatial orientation, and position, this candidate, which we call Sgr 1, is almost certainly associated with the Sagittarius stream system, in particular, with the trailing arm. To fully confirm this, and to compare our detection with the stream models available, it would be beneficial to measure line-of-sight velocities of the RRab stars within the bounds of the sub-structure. The second most significant overdensity candidate, with a significance of  $\sim 9\sigma$ , is located near the Galactic center. It is stretched over many tens of degrees in right ascension, which makes it difficult to pinpoint its origin. Finally, we present all the overdensity candidates found in our procedure with significances in excess of  $2\sigma$ . In order to confirm – or discard – these candidates, a wide-area imaging and spectroscopic survey is

necessary. Our highly complete catalog of the southern RR Lyrae fills in a large gap which has been so far precluding a detailed and unbiased analysis of the Galactic stellar halo, both in terms of its constituent sub-structure as well as its shape and extent.

## ACKNOWLEDGMENTS

We thank A. K. Vivas, S. Duffau, and the anonymous referee, for useful comments and discussions. Support for M.C. and G.T. is provided by the Ministry for the Economy, Development, and Tourism's Programa Inicativa Científica Milenio through grant IC120009, awarded to the Millennium Institute of Astrophysics (MAS); by Proyecto Basal PFB-06/2007; and by Proyecto FONDECYT Regular #1141141. Additional support for G.T. is provided by CONICYT Chile. CRTS and CSDR1 are supported by the U.S. National Science Foundation under grants AST-0909182 and CNS-0540369. The SSS survey is funded by the National Aeronautics and Space Administration under Grant No. NNG05GF22G issued through the Science Mission Directorate Near-Earth Objects Observations Program.

## REFERENCES

- An, D., Beers, T. C., Johnson, J. A., et al. 2012, in Aoki, W., Ishigaki, M., Suda, T., Tsujimoto, T., Arimoto, N., eds, ASP Conf. Proc. Vol. 458, Galactic Archaeology: Near-Field Cosmology and the Formation of the Milky Way. Astron. Soc. Pac., 2012., San Francisco, p.179
- Arce, H. G., & Goodman, A. A. 1999, ApJ, 512, L135

- Baart, M. L. 1982, IMA J. Num. Analysis, 2, 241
- Beers, T. C., Carollo, D., Ivezić, Ž., et al. 2012, ApJ, 746, 34
- Belokurov, V., Zucker, D. B., Evans, N. W., et al. 2006, ApJ, 642, L137
- Belokurov, V., Evans, N. W., Bell, E. F., et al. 2007a, ApJ, 657, L89
- Belokurov, V., Evans, N. W., Irwin, M. J., et al. 2007b, ApJ, 658, 337
- Belokurov, V. 2013, New Astronomy Reviews, 57, 100
- Belokurov, V., Irwin, M. J., Koposov, S. E., et al. 2014a, arXiv:1403.3406
- Belokurov, V., Koposov, S. E., Evans, N. W., et al. 2014b, MNRAS, 437, 116
- Bertin, E., & Arnouts, S. 1996, A&AS, 117, 393
- Bonifacio, P., Monai, S., & Beers, T. C. 2000, AJ, 120, 2065
- Boylan-Kolchin, M., Bullock, J. S., & Kaplinghat, M. 2011, MNRAS, 415, L40
- Bovill, M. S., & Ricotti, M. 2011, ApJ, 741, 18
- Brooks, A. M., & Zolotov, A. 2014, ApJ, 786, 87
- Bullock, J. S., Kolatt, T. S., Sigad, Y., et al. 2001, MNRAS, 321, 559
- Carretta, E., Bragaglia, A., Gratton, R., D'Orazi, V., & Lucatello, S. 2009, A&A, 508, 695
- Catelan, M., & de Freitas Pacheco, J. A. 1993, AJ, 106, 1858
- Catelan, M. 2009, Ap&SS, 320, 261
- Catelan, M., & Cortés, C. 2008, ApJ, 676, L135
- Deason, A. J., Belokurov, V., & Evans, N. W. 2011, MNRAS, 416, 2903
- Deason, A. J., Belokurov, V., Evans, N. W., & Johnston, K. V. 2013, ApJ, 763, 113
- Drake, A. J., Djorgovski, S. G., Mahabal, A., et al. 2009, ApJ, 696, 870
- Drake, A. J., Catelan, M., Djorgovski, S. G., et al. 2013a, ApJ, 763, 32
- Drake, A. J., Catelan, M., Djorgovski, S. G., et al. 2013b, ApJ, 765, 154
- Dressler, A. 1980, ApJ, 236, 351
- Duffau, S., Vivas, A. K., Zinn, R., Méndez, R., & Ruiz, M. T. 2014, A&A, 566, A118
- Eggen, O. J., Lynden-Bell, D., & Sandage, A. R. 1962, ApJ, 136, 748
- Fellhauer, M., Belokurov, V., Evans, N. W., et al. 2006, ApJ, 651, 167
- Freeman, K., & Bland-Hawthorn, J. 2002, ARA&A, 40, 487
- Grillmair, C. J. 2006, ApJ, 645, L37
- Guldenschuh, K. A., Layden, A. C., Wan, Y., et al. 2005, PASP, 117, 721
- Harding, P., Morrison, H. L., Olszewski, E. W., et al. 2001, AJ, 122, 1397
- Helmi, A., Cooper, A. P., White, S. D. M., et al. 2011, ApJ, 733, L7
- Ibata, R. A., Gilmore, G., & Irwin, M. J. 1994, Nature, 370, 194
- Jiang, I. G., & Binney, J. 2000, MNRAS, 314, 468
- Johnston, K. V., Hernquist, L., & Bolte, M. 1996, ApJ, 465, 278
- Jurcsik, J. 1995, AcA, 45, 653
- Jurcsik, J., & Kovács, G. 1996, A&A, 312, 111
- Jurić, M., Ivezić, Ž., Brooks, A., et al. 2008, ApJ, 673, 864
- Kinemuchi, K., Smith, H. A., Woźniak, P. R., McKay, T. A., & ROTSE Collaboration 2006, AJ, 132, 1202
- Kinman, T. D., Morrison, H. L., & Brown, W. R. 2009, AJ, 137, 3198
- Kinman, T., Castelli, F., Cacciari, C., et al. 2000, A&A, 364, 10
- Klypin, A., Kravtsov, A. V., Valenzuela, O., & Prada, F. 1999, ApJ, 522, 82
- Koposov, S. E., Yoo, J., Rix, H.-W., et al. 2009, ApJ, 696, 2179
- Koposov, S. E., Belokurov, V., Evans, N. W., et al. 2012, ApJ, 750, 80
- Koposov, S. E., Irwin, M., Belokurov, V., et al. 2014, arXiv:1403.3409
- Larson, S., Beshore, E., Hill, R., et al. 2003, BAAS, 35, 982
- Layden, A. C. 1997, AJ, 115, 193
- Layden, A. C. 1995, AJ, 110, 2312
- Law, D. R., & Majewski, S. R. 2010, ApJ, 714, 229
- Lomb, N. R. 1976, Ap&SS, 39, 447
- Majewski, S. R., Skrutskie, M. F., Weinberg, M. D., & Ostheimer, J. C. 2003, ApJ, 599, 1082
- Martin, N. F., Ibata, R. A., Rich, R. M., et al. 2014, arXiv:1403.4945
- Nemec, J. M. 2004, AJ, 127, 2185
- Nemec, J. M., Smolec, R., Benkő, J. M., et al. 2011, MNRAS, 417, 1022
- Nemec, J. M., Cohen, J. G., Ripepi, V., et al. 2013, ApJ, 773, 181
- Newberg, H. J., Yanny, B., Rockosi, C., et al. 2002, ApJ, 569, 245
- Pawlowski, M. S., Pflamm-Altenburg, J., & Kroupa, P. 2012, MNRAS, 423, 1109
- Pawlowski, M. S., Kroupa, P., & Jerjen, H. 2013, MNRAS, 435, 1928
- Petersen, J. O. 1986, A&A, 170, 59
- Scargle, J. D. 1982, ApJ, 263, 835
- Schlegel, D. J., Finkbeiner, D. P., & Davis, M. 1998, ApJ, 500, 525
- Schwarzenberg-Czerny, A. 1989, MNRAS, 241, 153
- Schwarzenberg-Czerny, A. 1996, ApJ, 460, L107
- Schwarzenberg-Czerny, A., & Beaulieu, J. Ph. 2006, MNRAS, 365, 165
- Searle, L., & Zinn, R. 1978, ApJ, 225, 357
- Sesar, B., Ivezić, Ž., Grammer, S. H., et al. 2010, ApJ, 708, 717
- Sesar, B., Grillmair, C. J., Cohen, J. G., et al. 2013, ApJ, 776, 26
- Simion, I. T., Belokurov, V., Irwin, M., & Koposov, S. E. 2014, MNRAS, 440, 161
- Smolec, R. 2005, AcA, 55, 59
- Starkenburger, E., Helmi, A., De Lucia, G., et al. 2013, MNRAS, 429, 725
- Szczygieł, D. M., Pojmański, G., & Pilecki, B. 2009, AcA, 59, 137
- Tolstoy, E., Hill, V., & Tosi, M. 2009, ARA&A, 47, 371
- Vivas, A. K., Zinn, R., Andrews, P., et al. 2001, ApJ, 554, L33
- Vivas, A. K., & Zinn, R. 2006, AJ, 132, 714
- Vivas, A. K., Jaffé, Y. L., Zinn, R., et al. 2008, AJ, 136, 1645
- Wang, J., Frenk, C. S., & Cooper, A. P. 2013, MNRAS, 429, 1502
- Watson, C. L. 2006, Society for Astronomical Sciences An-

- nual Symposium, 25, 47  
 Weisz, D. R., Dolphin, A. E., Skillman, E. D., et al. 2014, arXiv:1405.3281  
 Welch, D. L., & Stetson, P. B. 1993, AJ, 105, 1813  
 Willman, B. 2010, Advances in Astronomy, 2010  
 Yanny, B., Newberg, H. J., Johnson, J. A., et al. 2009, ApJ, 700, 1282  
 Zinn, R., & West, M. J. 1984, ApJS, 55, 45  
 Zorotovic, M., Catelan, M., Smith, H. A., et al. 2010, AJ, 139, 357; erratum: AJ, 140, 912